Optical Frequency Domain Reflectometry Based Quasi-distributed High Temperature Sensor

Nan Wu

Thesis submitted to the faculty of the
Virginia Polytechnic Institute and State University
in partial fulfillment of the requirements for the degree of

Master of Science
In
Electrical Engineering

Anbo Wang, Chair
Gary R. Pickrell
Yizheng Zhu

December 9, 2013
Blacksburg, VA

Keywords: OFDR, high temperature, multiplexed, direct-bonding, signal demodulation

Copyright 2013, Nan Wu

Optical Frequency Domain Reflectometry Based Quasi-distributed High Temperature Sensor

Nan Wu

ABSTRACT

Temperature sensing in harsh environment is desired in many areas, such as coal gasification, aerospace, etc. Single crystal sapphire is an excellent candidate for construction of harsh environment sensors due to its superior mechanical and optical properties even at temperature beyond 1600 ℃.

The temperature inside a coal gasifier can be as high as 1200 ℃. And there is dramatic temperature gradient between the inner and outer layers of the gasifier refractory. Previous work has been done at Virginia Tech's Center for Photonics Technology to design and fabricate a sapphire wafer based Fabry-Perot interferometer (FPI) sensor for temperature sensing in coal gasifiers. The sensor head is based on the use of sapphire wafer which is attached to a lead-in sapphire fiber to be applied in the ultrahigh temperature region; and the sapphire fiber is spliced to a multi-mode fused silica fiber for quality signal transmission in lower temperature areas. One of the challenges encountered by this approach is the shear force to the sapphire fiber, which is caused by the differential thermal expansion between the inner and outer layers of the gasifier refractory. This shear force may be so significant to break the sensor probe. This thesis proposed a free space based interrogation sensing system to address that problem. In this free space based interrogation sensing system, only the sensor head is placed in the inner refractory wall, while all the other parts of the system are placed in the outer refractory or outside the gasifier at the ambient room temperature. An optical frequency domain reflectometry (OFDR) based multiplexed technique is applied in the sensor design to realize temperature measurement at multiple locations along the optical path. In this work, three sapphire wafers based multiplexed temperature sensor is fabricated and calibrated in laboratory. This multiplexed high temperature sensor shows linear response in the range of 20 ℃ ~ 1000 ℃, with a sensitivity of $1.602 \times 10^{-5}/°\mathrm{C}$ and a resolution of 1.3°C.

Acknowledgements

First of all, I would like to express my deepest gratitude and appreciation to my advisor, Dr. Anbo Wang, for offering me this great opportunity to work and study at the Center for Photonics Technology (CPT) with such a wonderful team. I am indebted for his consistent support, inspiration and encouragement during this one and half years. I would also like to thank my other committee members, Dr. Gary Pickrell and Dr. Yizheng Zhu for their valuable suggestions and unreserved support.

I would also like to thank Dr. Bo Dong and Dr. Zhihao Yu for their generous assistance and suggestions on my research.

I also have to thank Mr. Donald Leber, the cleanroom manager in the Bradley Department of Electrical and Computer Engineering, for his kind help in the cleanroom training and fabrication. I am grateful for his guidance and support.

Special thanks also go to the CPT family, in particular to Zhipeng Tian, Chaofang Wang, Crystal Wang, Lingmei Ma, Di Hu, and Michael Fraser, for their help, encouragement, and friendship over the past one and half years. I have had a great time with all the CPT members. I feel fortunate and happy to work with them.

In addition, I would like to thank my dearest friends: Xinxin Liu and Cuixia Huang. They are always there for me, just like my family. I would not have survived without their supports and love.

Finally, I would like to give my biggest thanks to my parents for their endless supports and encouragement during my whole life.

Table of Contents

Acknowledgements iii

Table of Contents iv

List of Figures vi

Chapter 1 Introduction 1

1.1 Temperature Sensing 1

1.2 Motivation 2

1.3 Organization of Thesis 3

Chapter 2 Sensing Method Principles and Sensor Design 4

2.1 Fabry-Perot Interferometry 4

2.2 OFDR based Multiplexed Sensing Technique 6

2.2.1 Fundamental Concept of OFDR Technique 7

2.2.2 Applications of C-OFDR 9

2.3 Design of Interrogation System 9

2.4 Design of Sensor Head 10

2.5 Signal Processing 14

2.6 Simulation of the Sensing Principle 20

Chapter 3 Sensor Head Fabrication 29

3.1 Sensor Head Materials 29

3.2 Sensor Head Fabrication 30

3.2.1 Etching of the Well 30

3.2.2 Direct Bonding 37

Chapter 4 Evaluation of Sensor Performance 40

4.1 Experimental Test Setup 40

4.2 Signal Demodulation 41

4.3 Feasibility of Long Distance Interrogation 44

Chapter 5 Conclusion and Future Work 47

5.1 Summary of Work 47

5.2 Suggestions for Future Work 48

References 49

List of Figures

Figure 2-1: Basic structure of Fabry-Perot Interferometer [11] ‘used under fair use, 2013’ 4

Figure 2-2: Optical interrogation system for the frequency-multiplexed sensing [13] ‘used under fair use, 2013’ 6

Figure 2-3: FFT result of the three-sensor multipoint sensing system [13] ‘used under fair use, 2013’ 7

Figure 2-4: Fundamental principle of the OFDR technique [19] ‘used under fair use, 2013’ 8

Figure 2-5: Interrogation system for this quasi-distributed temperature sensing 9

Figure 2-6: Structure of sensor head 10

Figure 2-7: Interrogation system schematic for the preliminary experiment 12

Figure 2-8: Reflection spectrum during a wavelength scan.. 12

Figure 2-9: FFT of the reflection spectrum in spatial domain 13

Figure 2-10: Temperature responses for all seven sensing surfaces (left) and normalized temperature responses (right)... 13

Figure 2-11: Final structure of sensor head 14

Figure 2-12: A general OFDR based sensor head structure 21

Figure 2-13: Schematic of sensor head structure in the simulation example 24

Figure 2-14: Reflection spectrum during a wavelength scan... 26

Figure 2-15: Reflection spectrum in spatial domain... 27

Figure 2-16: Recovered spectrum for the last sensing surface 27

Figure 2-17: Temperature response for all four sensing surfaces (left) and normalized temperature response (right) 28

Figure 3-1: Illustration of the reflection from each surface 31

Figure 3-2: Sensor head structure for simulation on the impact of da 32

Figure 3-3: FFT results for $da = 0.8\mu m$ (upper left), $1.5\mu m$ (upper right), $0.4\mu m$ (lower left), $1.2\mu m$ (lower right)... 33

Figure 3-4: Simplified illustration of photolithography... 34

Figure 3-5: (a) Spin coater; (b) MA6 mask aligner; (c) Photo-mask............................... 35

Figure 3-6: Trion MiniLock reactive ion etching system 36

Figure 3-7: Configuration of sapphire wafers and masks for RIE................................... 37

Figure 3-8: Bonding results: sapphire sensor head (left), fused silica wafers (right) 39

Figure 4-1: Structure of sapphire wafer based sensor head 40

Figure 4-2: Schematic of experiment setup for temperature calibration 41

Figure 4-3: Reflection spectrum of the sensor measured at room temperature 41

Figure 4-4: Reflection spectrum of the sensor in spatial domain 42

Figure 4-5: Recovered spectra for all three sensing surfaces 42

Figure 4-6: Temperature response curves for the multiplexed sensor............................. 43

Figure 4-7: Normalized temperature response curves 43

Figure 4-8: Reflection spectrum of this long distance interrogation 45

Figure 4-9: FFT of the reflection spectrum.. 45

Chapter 1
Introduction

The field of fiber optical sensing began to take off in the late 1970s [1, 2]. Fiber optical sensors have shown many advantages over traditional electronic sensors, such as compact size and light weight, intrinsic immunity to electromagnetic interference (EMI), electrical and chemical passivity, high resolution, large dynamic range, potential of dense multiplexing, and capability of extremely long distance remote measurement. They are especially suitable for harsh environment sensing which may involve electrical hostile, ultrahigh temperature or corrosion where electronic sensors may be difficult to apply.

Fiber optical sensors can generally be grouped into two basic classes: intrinsic sensors and extrinsic sensors. The intrinsic fiber optical sensors are all fiber based sensing system; while an extrinsic sensor is a hybrid fiber optical sensor, where the fiber functions to transmit the optical signal other than to function as the sensing element, which is within the scope of this thesis.

Regarding the sensing range, the fiber optic sensors are generally classified into three categories: single point sensors, quasi-distributed sensors, and fully-distributed sensors. The sensor scheme proposed in this thesis is quasi-distributed.

In some applications, distributed information at multiple spots is more desired than just at a single point, which calls for the study on multiplexed sensing techniques.

1.1 Temperature Sensing

Temperature is among one of the most desired measurands in many applications such as in coal gasifiers, automated production plants, and high performance processors. Traditional low-cost electronic temperature sensors such as thermocouples, thermal resistors, and resistance temperature detectors (RTD) do not always show good performance, especially in the presence of electromagnetic interferences, chemical and mechanical disturbances. Fiber optical temperature sensors are more desired in such

harsh environment sensing. Most reported fiber optical temperature sensors are based on fiber interferometry [3-5] and Fiber Bragg Gratings (FBG) [6-8]. Among these methods, Fabry-Perot interferometric (FPI) sensors have a relatively simple configuration, and are efficient at temperature sensing with high accuracy and resolution, and easy to implement. FPI based sensors also have potential capability for multiplexing. The signal demodulation methods for such sensors are well-developed.

1.2 Motivation

The coal gasification technique is developed to convert coal into clean electricity, hydrogen, and other valuable energy products. The operating temperature in the coal gasifier is usually in the range of 1200 ℃ ~ 1600 ℃, depending on the physical locations in the chamber [9]. Real-time accurate and reliable measurement of temperature during the coal gasification process is essential for safe, efficient, and cost-effective operation. In the meantime, extreme chemical corrosion could cause significant progressive thinning of the inner refractory. If a sensor probe is surface or flush mount installed, the refractory thinning may lead to the loss of the sensor tip and thus disenable the intended measurement. It is therefore important to have a sensor that allows temperature measurement at different depths of the sensor insertion so temperature information can be continuously obtained even when the far most sensor tip is lost due to the corrosion.

Previous work has been done at the Center for Photonics Technologies (CPT) in Virginia Tech to design and fabricate a sapphire wafer based Fabry-Perot interferometer (FPI) sensor for temperature measurement in a coal gasifier, and field tests have been carried out. A piece of sapphire wafer is used as the sensing element, which is attached to a lead-in sapphire fiber to be applied in the ultrahigh temperature region; and the sapphire fiber is spliced to a multi-mode fused silica fiber for quality signal transmission in the lower temperature region. During a field test, the sensor probe that contains the sapphire fiber is inserted into a gasifier through the outer and inner refractory walls of a gasifier. However, the differential vertical thermal expansion of the refractory walls tends to break the sensor probe and thus reduce the sensor’s work life.

Regarding the above consideration, a free space based interrogation sensing system is proposed in this thesis to address the above problem. In this free space based interrogation sensing system, only the sensor head needs to be placed at the desired location, while all other parts of the interrogation system can be placed at a sufficiently long distance away from the gasifier-inner refractory. As compared to the single point temperature sensing in the previous works, this proposed sensor designed based on the OFDR sensing principle is a multiplexed temperature sensor. Three pieces of sapphire wafers are used to fabricate the sensor head by applying the direct wafer bonding technique. The feasibility of multiplexed sensing principle is experimentally demonstrated in laboratory.

1.3 Organization of Thesis

This thesis is organized into five chapters. Introduction and motivation are outlined in Chapter 1. Chapter 2 covers the sensing method principles and the detailed sensor design. The signal processing method will be introduced, and an example of simulation result will be shown in this chapter. The fabrication processes of the sensor head will be presented in detail in Chapter 3. Chapter 4 presents the temperature calibration results and experimental study on the feasibility of long distance interrogation. Finally, Chapter 5 concludes the work of this thesis and provides possible improvements and suggestions for future study on this subject.

Chapter 2
Sensing Method Principles and Sensor Design

In this thesis, a quasi-distributed high temperature sensor is studied. The sensor head can be simply treated as multiplexed Fabry-Perot cavities. The basic principle for Fabry-Perot Interferometry (FPI) will be introduced in Section 2.1, followed by the background of an OFDR based multiplexed sensing technique in Section 2.2. Sections 2.3 and 2.4 will present the design of the free space based interrogation system and the design of the sensor head. The signal demodulation method will be discussed in Section 2.5, and a simulation example will be given in Section 2.6 to illustrate the sensing principle step by step.

2.1 Fabry-Perot Interferometry

The Fabry-Perot interferometer (FPI) has a very simple configuration. The core element in the Fabry-Perot interferometry is a Fabry-Perot (FP) cavity consisted of two partially reflective reflectors placed mutually parallel, or a single transparent plate with two parallel reflecting surfaces [10], as shown in Figure 2-1. The length of the FP cavity is *L*, and the cavity is filled with a medium of refractive index *n*. r_1 and r_2 are the amplitude reflection coefficients of the two reflectors, respectively. Light is normally incident in our case.

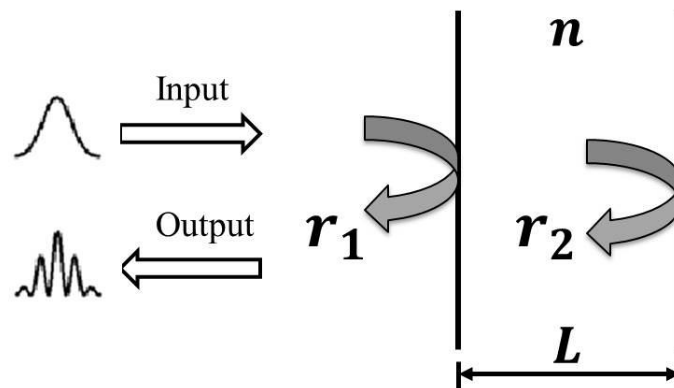

Figure 2-1: Basic structure of Fabry-Perot Interferometer [11] ‘used under fair use, 2013’

Multiple reflections will occur within the cavity, and two compensate interference patterns will be formed outside the two sides of the FP cavity when a monochromatic incident light applies. The interference spectrum is wavelength-dependent. In most sensor applications, the finesse, as defined in Equation (2.1), is low, higher order reflections can be neglected; and the expression of the reflected spectrum is then simplified as the interference of two first-order reflection beams, as shown in Equation (2.2). The noise is not included in Equation (2.2).

$$\mathcal{F} = \frac{\pi\sqrt{|r_1 r_2|}}{1-|r_1 r_2|} \tag{2.1}$$

$$I_r(\lambda) = I_1(\lambda) + I_2(\lambda) + 2\sqrt{I_1(\lambda) I_2(\lambda)} \cos(\frac{2\pi OPD}{\lambda} + \phi_0) \tag{2.2}$$

ϕ_0 is the initial phase shift; OPD is the optical path difference for light traveling a round trip within the FP cavity, which is temperature dependent in the application of temperature sensing.

$$OPD(T) = 2n(T)L(T) \tag{2.3}$$

In temperature sensing, the OPD of the FP cavity will change with temperature mainly due to two factors: the thermal expansion of the cavity length, and the thermal-sensitive refractive index of the medium between the two reflectors. The change of OPD regarding the temperature is described by Equation (2.4) [12], where α_n is the 1st order thermal coefficient of the refractive index for the medium within the cavity; α_l is the 1st order coefficient of thermal expansion for the medium thickness of the cavity. Usually the materials used as the sensing element in the temperature sensing applications have positive values for α_d and α_l. Thus the OPD of the FP cavity will go up as temperature increases.

$$\frac{OPD(T)}{OPD(T_0)} = \frac{2n(T)L(T)}{2n(T_0)L(T_0)} \approx 1 + (\alpha_n + \alpha_l)(T - T_0) \tag{2.4}$$

In real sensing applications, a broad-band light source or a continuously tunable laser is used in the interrogation system. The frequency of the reflected spectrum is given by the temperature-dependent OPD, which will be demodulated from the reflected spectrum with certain signal processing algorithms, which will be discussed in detail in Section 2.5. By detecting the change of OPD, we can obtain the temperature information based on the sensor calibration. This is the basic principle of the FPI based temperature sensing technique.

2.2 OFDR based Multiplexed Sensing Technique

As mentioned in Chapter 1, multiplexed sensing is desired in many applications. The basic principle of the FPI based sensing technique can be extended to a multiplexed sensing system, as long as each FP sensor can be distinguished from each other.

As seen in Equation (2.2), the FPI based temperature sensor is characterized by its temperature-dependent OPD value, which can also be treated as the frequency of the sensor's interference fringes. Thus an intuitive way to realize the multiplexed temperature sensing is to make multiple in-line FP sensors with different OPDs, and each sensor can be distinguished in the spatial domain by taking fast Fourier transform (FFT) of the total reflected spectrum. A multiplexed high temperature sensing system consisted of three sapphire fiber air gap-based extrinsic FPI sensors is reported in [13], as shown in Figure 2-2. The demultiplexing of the sensors can be achieved by taking FFT of the detected spectrum, each peak in the FFT spectrum corresponds to a sensor's OPD (Figure 2-3).

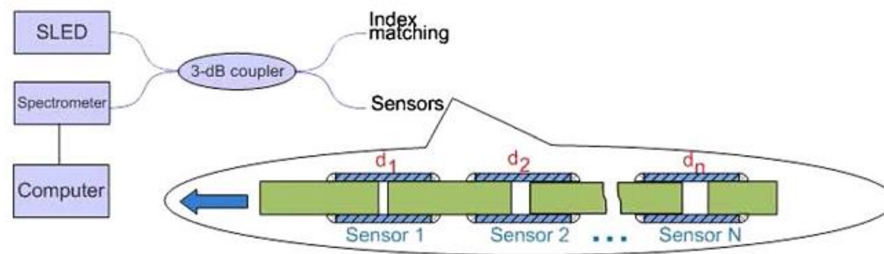

Figure 2-2: Optical interrogation system for the frequency-multiplexed sensing [13] 'used under fair use, 2013'

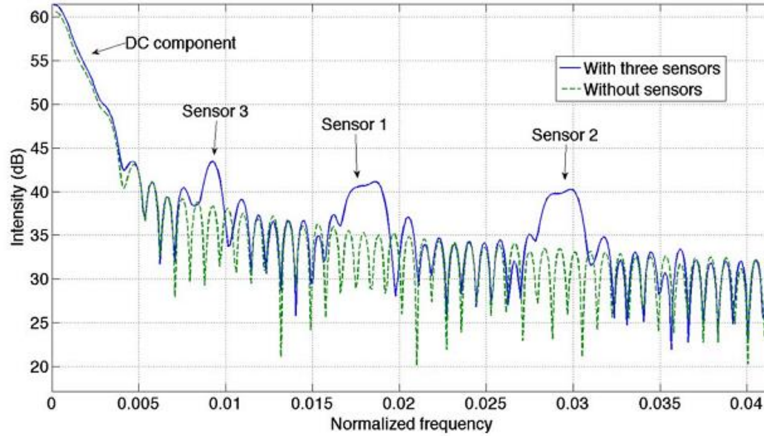

Figure 2-3: FFT result of the three-sensor multipoint sensing system [13] 'used under fair use, 2013'

In the frequency-multiplexed sensing system discussed above, each sensor must have a unique OPD value to avoid potential cross-talk between sensors. The work involved in this thesis introduces a different multiplexing system in which identical OPD values are allowed as long as long as all sensors are placed in different distances from the reference reflector. This sensing system is based on the Optical Frequency Domain Reflectometry (OFDR) technique.

2.2.1 Fundamental Concept of OFDR Technique

The OFDR method has been reported since 1981 [14-17] as an alternative technique to the optical time domain reflectometer (OTDR) for its capability of higher spatial resolution and sensitivity, and falls into two main categories: incoherent OFDR (I-OFDR) and coherent OFDR (C-OFDR) [18]. The C-OFDR technique is based on the measurement of the beat signal formed by the interference between reflections from the Device Under Test (DUT) and a fixed reference reflection (also called Local Oscillator (LO)) in the frequency (wavelength) domain, which will be applied to our proposed sensing system.

Figure 2-4 shows a basic schematic of a C-OFDR based sensing system. A tunable laser is used as the light source whose optical frequency is linearly swept in time without mode hops. Light coming out of the tunable laser source (TLS) is split into two beams through a fiber coupler. One beam is used to probe the DUT, and the other is connected with the reference reflector. The reflections from reflectors in the DUT will beat with the fixed reference reflection, and the interference signal is detected by the photodiode. The beat frequencies are proportional to the distance between reflection points in the DUT and the LO. The location information of the reflectors in the DUT can be extracted by taking FFT of the beat spectrum.

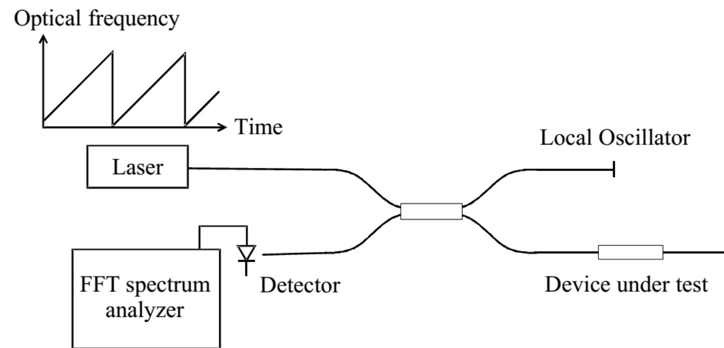

Figure 2-4: Fundamental principle of the OFDR technique [19] 'used under fair use, 2013'

In the C-OFDR technique, the state of polarization (SOP) of the back-reflected light signal will strongly affect the intensity of the measured signal [20]. If the SOP of the reference reflection and the test signals are orthogonal at the detector, no beat signal will be detected. The SOP of the light signal will change unpredictably when transmitting along the optical fiber due to the birefringence of the fiber. Thus the polarization controllers should be employed in order to control the SOP of the reference or test light beams. However, it is still very hard to obtain precise measurements when there are multiple reflections in the test arm. In [21], a solution by applying a polarization diversity receiver is proposed to avoid the polarization dependence. The sum of the test and reference signals is split into two orthogonal polarization states, and two photo-detectors are employed to receive the two polarization states respectively. In [20], another solution

is employed by repeating a great number of measurements while changing the SOP of the reference reflection and retaining the maximum signal intensity at the detector. This method requires less electronics and optical components, but is time consuming.

In this thesis, the challenge of the polarization dependence in C-OFDR will be well avoided by arranging the reference arm and the test arm in line. Detailed design will be introduced in the later section.

2.2.2 Applications of C-OFDR

The C-OFDR technique has found its way in many different applications. Some typical applications include: optical components and modules [22, 23], measurement of distributed birefringence in optical fibers [24-26], distributed sensing systems [27], biomedical imaging [28], etc.

2.3 Design of Interrogation System

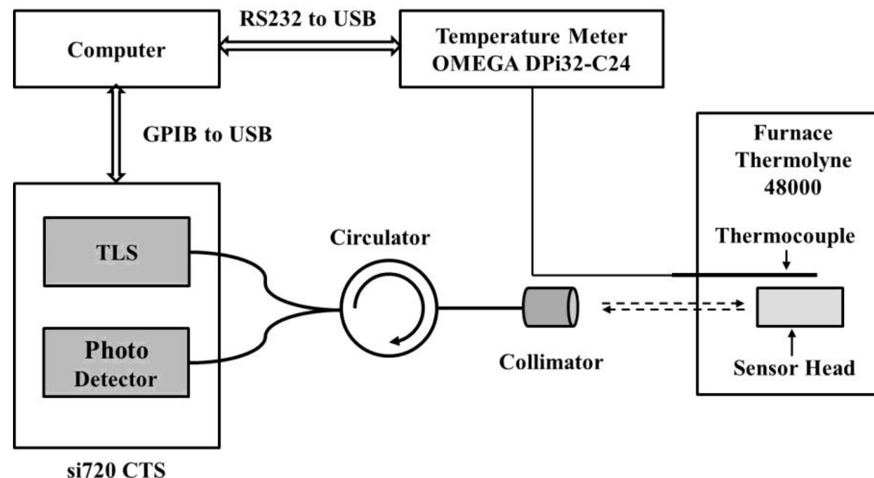

Figure 2-5: Interrogation system for this quasi-distributed temperature sensing

As mentioned in Chapter 1, the interrogation system proposed in this thesis is free-space-based, as shown in Figure 2-5. Light coming from the Micron Optics si720 Component Testing System (CTS) propagates through a fiber circulator to the collimator, and the collimated light beam is then shooting onto the sensor head. The reflected signal is then

coupled back into the collimator, and again propagates through the fiber circulator back to the CTS.

The Micron Optics si720 Component Testing System (CTS) has a built-in tunable laser and a detector. The built-in tunable laser of the CTS has a tuning range from 1520nm to 1570nm with a sweeping frequency of 5Hz, and a resolution of 2.5pm. The wavelength repeatability and accuracy are 0.05pm and 1pm, respectively. The spectral data can be easily transferred to the computer via GPIB interface. The sensor head is placed in a furnace (Thermolyne 48000). A thermocouple is placed adjacently to the sensor head as the temperature reference. The temperature readings are acquired by the computer from the temperature gauge (OMEGA Dpi32-C24) via RS232 to USB cable.

2.4 Design of Sensor Head

As mentioned in Section 2.2.1, the reference arm and the test arm are arranged in line. Our basic idea is to use a stack of double-side-polished transparent wafers as the sensor head, and the front surface of the first wafer is used as the reference reflector. Considering the consistency of the thermal expansion, all wafers are of the same material. Assuming the coherent length of the TLS can cover the whole range of the sensor head, the interference will occur between each two reflectors. Interferences between each two reflectors have frequencies that are governed by the physical separation of those two reflectors. To distinguish the reference-sensor interferences from the inter-sensor interferences, the thickness of the first wafer must be chosen as not equal to or multiples of the thicknesses of other wafers given that other wafers have an identical thickness, as seen in Figure 2-6.

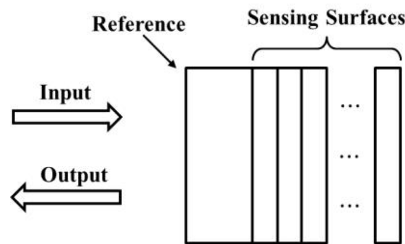

Figure 2-6: Structure of sensor head

The choice of sensor head material mainly depends on the sensing environment. The sensor head material should maintain both good mechanical and optical properties throughout the whole temperature range to be measured. Fused silica and single crystal sapphire are two most common commercially available sensor materials. Fused silica wafers will become soft and degrades in mechanical properties when operation temperature exceeds 1000 ℃ [29], thus cannot be employed in the ultrahigh temperature sensing system; however, it is still a good choice for the feasibility study of the OFDR based multiplexed sensing principle. In practical applications, a single crystal sapphire wafer is a better candidate for harsh environment sensing with ultrahigh temperature involved like coal gasifier as discussed in Chapter 1, as it can potentially maintain good performances at ultrahigh temperatures as up to 2000 ℃.

The major challenge in this sensor head fabrication is how to bond wafers together. Considering the target temperature range and requirement on consistency of the materials' thermal expansion, direct bonding of the wafers is a reliable choice as there will be no other materials involved. The bonding between two adjacent surfaces will greatly affect the sensing quality as can be seen in the following example.

Before we proceed to the sensor fabrication technique, a preliminary experiment was conducted for the feasibility study of this sensing principle, providing us some scopes in further studies.

A piece of reference glass with thickness of around 5.8mm and six pieces of microscope slides with thickness of around 1.1mm available in our lab were used to constitute the sensor head in this preliminary experiment. These glasses were simply bonded by water, and tested in the furnace from 30 ℃ to 90 ℃. Since the reference glass had a different thickness from all other sensing glasses, the seven sensing surfaces were at different distances away from the reference surface.

The interrogation system schematic is shown in Figure 2-7, which is the same as we discussed in Section 2.3. The CTS was used as both the TLS and the photo detector. The

measured reflection spectrum is shown in Figure 2-8, and its corresponding FFT spectrum in spatial domain is shown in Figure 2-9. All the marked peaks are from the reference-sensor interferences.

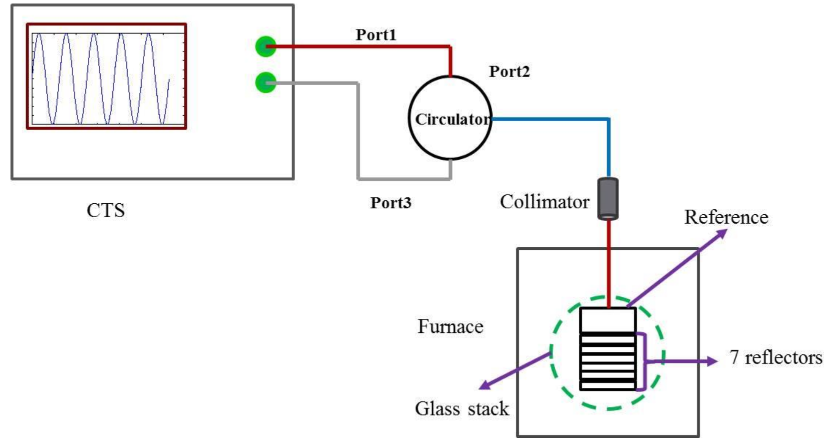

Figure 2-7: Interrogation system schematic for the preliminary experiment

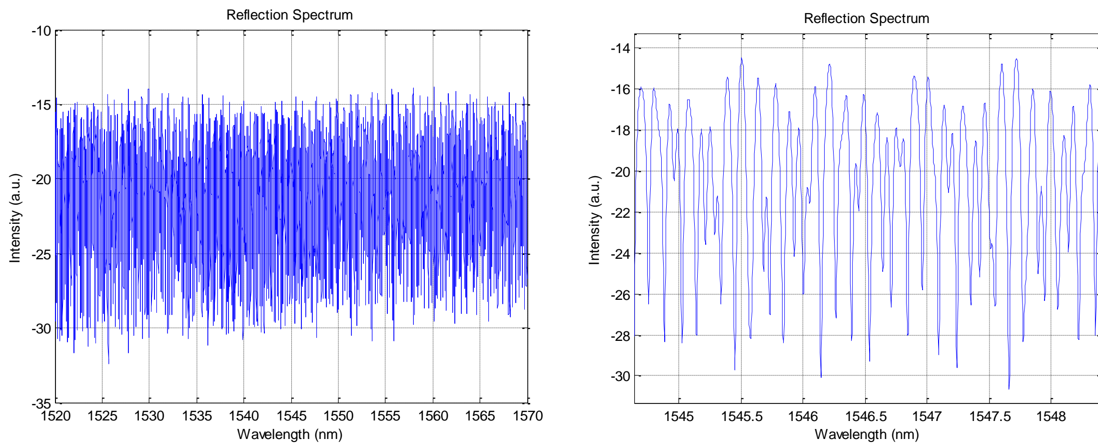

Figure 2-8: Reflection spectrum during a wavelength scan

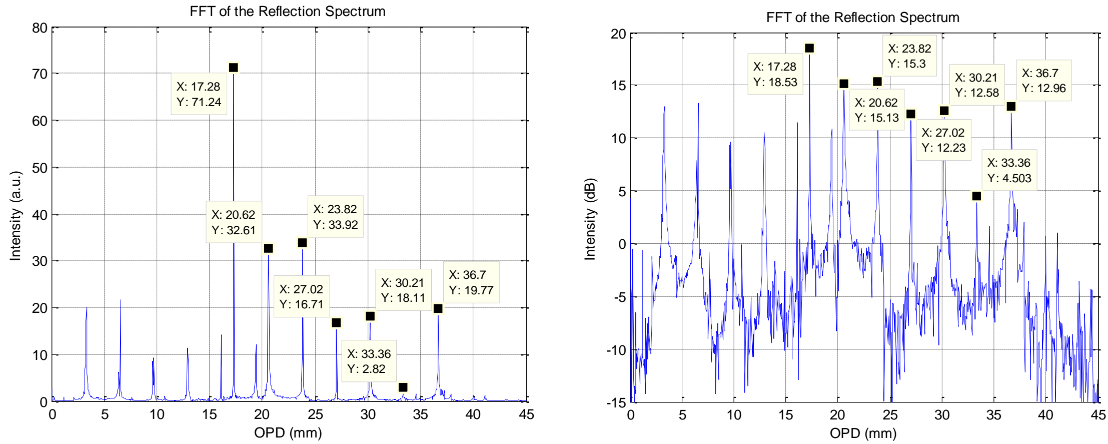

Figure 2-9: FFT of the reflection spectrum in spatial domain

By applying a certain signal demodulation method which will be discussed in the next section, the temperature responses for all the seven sensing surfaces are shown in Figure 2-10 (left). Normalized temperature response curves for these sensors can be obtained by normalizing their response curves to the corresponding OPD values at the first temperature which is around 30 ℃, as shown in Figure 2-10 (right).

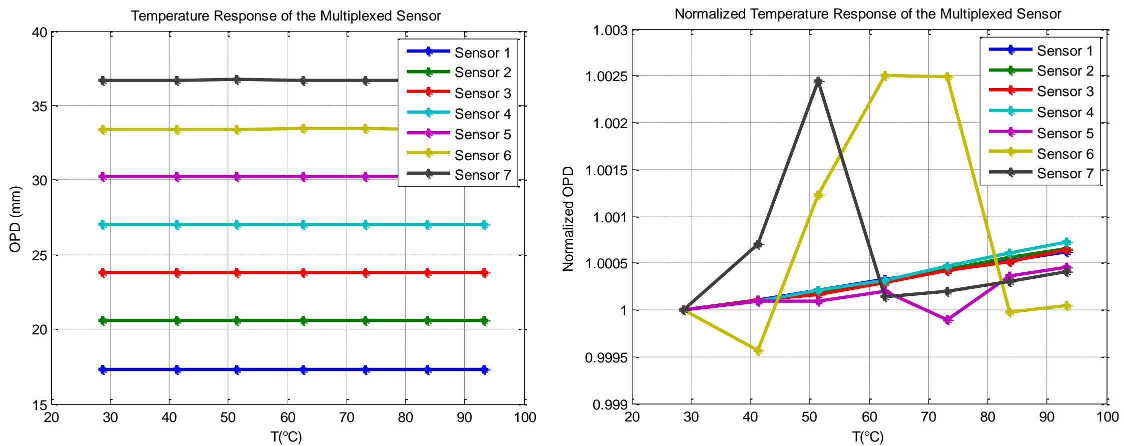

Figure 2-10: Temperature responses for all seven sensing surfaces (left) and normalized temperature responses (right)

We can find that sensor 1 to sensor 4 have an approximately identical linear normalized temperature response curve, while sensor 5 to sensor 7 show bad performances. Careful

examination on the sensor head shows that the bad performances of sensors 5 to 7 may be caused by poor bonding, as there are obvious air gaps between those glasses which would oscillate during the temperature measurement, causing the unpredictable jumps of the sensors' OPD value.

The above preliminary experimental results show the great impact of the bonding quality on the sensor's performance. To avoid the unstable contact between two adjacent surfaces, direct wafer bonding will be employed in the sensor fabrication. The final structure of the sensor head is shown in Figure 2-11. A thin air cavity is first etched on one side of the sensing wafers before performing the direct bonding. Detailed fabrication processes will be discussed in Chapter 3.

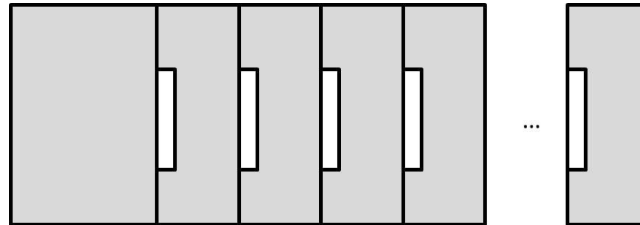

Figure 2-11: Final structure of sensor head

2.5 Signal Processing

As shown in Figure 2-6, we assume the thickness of the first wafer is d_0, while all other wafers have an identical thickness of d. Thus the distance between the reference and the jth sensing surface is given as $d_j = d_0 + (j-1)d$. Assume the coherent length of the CTS is longer than the span of the sensor head, and thus interference will occur between each two reflectors of the sensor head.

Assume the reflectance of the normal incidence on the interface between the sensor head material and the air is far less than one (which is true for both fused silica wafer based sensors and sapphire wafer based sensors); higher order reflections can then be neglected. The total light intensity received by the detector of the CTS can be simplified as Equation (2.5), where E_0 is the amplitude of the reflected electric field from the reference, E_j is the

amplitude of the reflected electric field from the jth sensing surface, d_j is the distance between the reference and the jth sensing surface, n is the reflective index of the sensor head material.

$$I_r(\lambda)=\left|E_0\exp(-j\pi)+\sum_{j=1}^{n}E_j\exp\left(-j\frac{4\pi n(T)d_j(T)}{\lambda}\right)\right|^2 \tag{2.5}$$

Since each sensing surface has a different distance from the reference reflector, the interference of the light reflected by each sensing surface and the reference signal will have different beat frequencies, which can be interpreted in the spatial domain by taking FFT of the detected spectrum. Algorithms used to demodulate the OPD value for a single FPI based sensor can be extended to this OFDR based multiplexed sensing system by using a band-pass filter to select a particular sensor in the spatial domain.

To illustrate the above principle, we take the simplest structure with only two pieces of wafers as an example. In this case, the sensor head has three reflectors including the reference surface. Equation (2.5) becomes

$$I_r(\lambda)=\underbrace{(I_0+I_1+I_2)}_{DC}+\left\{\underbrace{\begin{array}{l}2\sqrt{I_0I_1}\cos\left(\dfrac{4\pi n(T)d_1(T)}{\lambda}-\pi\right)\\ +2\sqrt{I_0I_2}\cos\left(\dfrac{4\pi n(T)d_2(T)}{\lambda}-\pi\right)\\ +2\sqrt{I_1I_2}\cos\left(\dfrac{4\pi n(T)\left(d_2(T)-d_1(T)\right)}{\lambda}\right)\end{array}}_{AC}\right\} \tag{2.6}$$

It is clear that the detected signal has both DC and AC components, of which only the AC component is of interest to us. There are three different frequencies included in the AC component, as seen in Equation (2.6). The first one comes from the interference of the

reference and the first sensing surface; the second one comes from the interference of the reference and the second sensing surface; and the last one comes from the interference of the two adjacent sensing surfaces. As previously mentioned, d_1 is the physical distance between the first sensing surface and the reference surface, which is also equal to the thickness of the first wafer d_0; d_2 is the physical distance between the second sensing surface and the reference surface; $d = d_2 - d_1$ is the thickness of the second wafer, which is different from d_0; and n is the refractive index of the sensor material. As the measurement of this temperature-dependent refractive index n is not within the scope of this thesis, we calibrate the temperature response of the OPD value instead of the physical length of the sensor. To be specified, $OPD_1 = 2nd_1$ and $OPD_2 = 2nd_2$ are the desired information that can be readily separated by digital filters and obtained by applying a certain algorithm which will be discussed in detail later.

For a single FP sensor, the detected reflection signal is described by Equation (2.2). Filtering out the DC component and normalizing the signal will yield the AC component only as:

$$I_{AC}(\lambda, T) = \cos\left(\frac{2\pi OPD(T)}{\lambda} + \phi_0\right) \tag{2.7}$$

In the reflection spectrum, two adjacent peaks at λ_1 and λ_2 (suppose $\lambda_2 > \lambda_1$) should satisfy the following equations:

$$\begin{cases} \dfrac{2\pi OPD}{\lambda_1} + \phi_0 = 2\pi \cdot N \\ \dfrac{2\pi OPD}{\lambda_2} + \phi_0 = 2\pi \cdot (N-1) \end{cases} \tag{2.8}$$

The OPD value can be obtained from Equation (2.8) as:

$$OPD = \frac{\lambda_1 \lambda_2}{\lambda_2 - \lambda_1} \tag{2.9}$$

The relative error of this method is given by Equation (2.10) [30], which is relatively large.

$$\frac{\Delta OPD}{OPD} \cong \sqrt{2}\left|\frac{\lambda_2}{\lambda_1-\lambda_2}\right|\left|\frac{\Delta\lambda_1}{\lambda_1}\right| \tag{2.10}$$

The mth peak of the wavelength λ_m satisfies:

$$\frac{2\pi OPD}{\lambda_m}+\phi_0 = 2\pi\cdot m \tag{2.11}$$

The above equation gives the OPD as:

$$OPD = \left(m-\frac{\phi_0}{2\pi}\right)\lambda_m \tag{2.12}$$

The relative error of this method can be approximately as:

$$\frac{\Delta OPD}{OPD} \cong \frac{\Delta\lambda}{\lambda} \tag{2.13}$$

As compared to Equation (2.10), this method has a better resolution, yet coming with the ambiguity problem. In [30], these two techniques are combined to demodulate the OPD value, which is also known as the peak-tracking method. This method can be applied to all peaks and valleys in the whole spectrum range, and a more accurate calibration can be obtained by using the averaged OPD value.

However, for FP sensor with a relatively long cavity which is the case in this thesis, there will be a lot of peaks and valleys which can make the peak-tracking method inefficient, and tracking only several peaks will lead to a relatively poor resolution.

Linear regression method proposed in [31] by Shen, which utilizes the whole spectrum with higher accuracy as compared to the peak tracking method, can be applied to a

system with a long FP cavity length, and can easily be extended to a multiplexed FPI sensing system.

As we discussed in Section 2.1, the detected spectrum of the single FPI contains both DC and AC components, where the DC component is the background spectrum, and the AC component is an amplitude-modulated (AM) term. Our goal is to demodulate the carrier frequency of the AM term, which is the OPD value. Shen's method is based on phase linear regression to estimate this carrier frequency of the analytical signals [31].

First convert the intensity of the AM signal from wavelength domain to wavenumber domain, and the corresponding analytical model is expressed as:

$$\tilde{I}_r(k) = I_0(k)\exp\left[j\left(k \cdot OPD + \phi_0\right)\right] \tag{2.14}$$

where the wavenumber $k = 2\pi/\lambda$.

Assume the frequency of the laser source is linearly modulated, thus the wavenumber is uniformly spaced. The filtered analytical signal is given as:

$$x_n = A_n \exp\left[j\left(k_n \cdot OPD + \phi_0\right)\right] + w_n,\ n = 1, 2, \ldots N \tag{2.15}$$

where A_n is the amplitude after filtering, k_n is the uniform spaced wavenumber, ϕ_0 is the initial phase, w_n is the residual white noise, and N is the total sample size.

The linear regression based frequency estimation given in [32] can be extended to this AM analytical signal model.

The unwrapped total phase of the analytical signal model in Equation (2.15) can be written as:

$$\begin{aligned} \Phi_n &= \tan^{-1}\left[\mathrm{Im}\left(x_n\right)/\mathrm{Re}\left(x_n\right)\right] + 2m\pi \\ &= k_n \cdot OPD + \phi_0 + \varepsilon_n \end{aligned} \tag{2.16}$$

where ε_n is the phase noise.

If we obtain a sequence of pairwise $\{\Phi_n, k_n\}$, a linear regression technique can be applied to estimate the *OPD* value and the initial phase term ϕ_0. The estimation can be achieved by the least-squares estimation which is to minimize the following sum of square error:

$$S = \sum_{n=1}^{N} \left[\Phi_n - k_n O\hat{P}D - \hat{\phi}_0 \right]^2 \tag{2.17}$$

The resulted estimation is given by:

$$\begin{bmatrix} O\hat{P}D \\ \hat{\phi}_0 \end{bmatrix} = \left(A^T A \right)^{-1} A^T \Phi \tag{2.18}$$

where

$$A = \begin{bmatrix} k_1 & k_2 & \cdots & k_N \\ 1 & 1 & \cdots & 1 \end{bmatrix}, \ \Phi = \begin{bmatrix} \Phi_1 & \Phi_2 & \cdots & \Phi_N \end{bmatrix}.$$

However the above unknown phase based estimation of OPD does not have very high precision, especially when the noise level is high. This estimation precision can be greatly improved by using a pre-calibrated initial phase since the phase term ϕ_0 would remain as a constant in practice. We denote this pre-calibrated phase term as $\tilde{\phi}_0$, and the estimation error of $\tilde{\phi}_0$ based on Equation (2.18) is:

$$\Delta\phi_0 = \hat{\phi}_0 - \tilde{\phi}_0 \tag{2.19}$$

Then the compensated frequency estimation for a known initial phase term $\tilde{\phi}_0$ can be given as:

$$O\tilde{P}D = O\hat{P}D + \Delta O\hat{P}D \tag{2.20}$$

$$\Delta O\hat{P}D = \left(C^T C \right)^{-1} C^T D \tag{2.21}$$

where

$$C = \begin{bmatrix} k_1 & k_2 & \cdots & k_N \end{bmatrix},\ D = \begin{bmatrix} \Delta\phi_0 & \Delta\phi_0 & \cdots & \Delta\phi_0 \end{bmatrix}.$$

As mentioned in Section 2.3, the CTS is used as our laser source, of which the wavelength is linearly swept instead of frequency. Thus we have to interpolate the measured spectra to be uniformly spaced in wavenumber domain.

The signal processing method for our multiplexed sensing system can be summarized as the following steps:

- Interpolate the measured spectra to have it sampled uniformly in the wavenumber domain.
- Perform one-side fast Fourier transform (FFT), and use a band-pass filter with a certain central frequency to select the desired frequency component and obtain the corresponding analytical signal.
- Obtain the unwrapped phase of the above analytical signal.
- Use Equation (2.18) to obtain an estimation of the OPD and initial phase term.
- For a known initial phase, use Equation (2.19) to obtain the phase difference.
- Use Equation (2.20) and (2.21) to obtain the compensated frequency estimation.
- Repeat the above steps for all other frequency components by simply applying band-pass filters with different central frequencies.

Following the above steps, the OPD information for all sensors will be successfully demodulated. By carefully recording the OPD values throughout the dynamic range of temperature, the calibration curve will be obtained.

2.6 Simulation of the Sensing Principle

In order to further explain the working principle of this OFDR based sensing system, a numeric simulation example will be provided in this section.

Before proceeding to a detailed example, we first show the general algorithm for calculating the exact reflection spectrum of such multi-layered structure with the Transfer Matrix Method.

A general OFDR based sensor structure as proposed in this thesis is shown in Figure 2-12. The reference wafer is represented by the purple layer, the sensing wafers are represented by the yellow layers, and all the etched air cavities are represented by the green layers. The first and last white blocks represent the incidence and transmitted space, respectively. The thickness of the nth layer is denoted as L_n, with permittivity and permeability as ε_n and μ_n, respectively. In our case, the permeability in all media is considered to be equal to the free space value, i.e. $\mu_i = \mu_1 = \cdots = \mu_n = \cdots = \mu_N = \mu_t = \mu_0$.

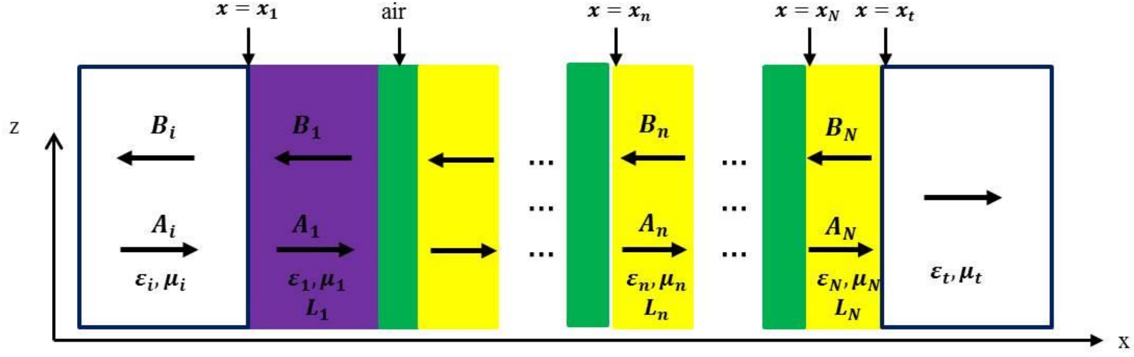

Figure 2-12: A general OFDR based sensor head structure

For normal incident TE wave, the EM field within the nth layer can be written as:

$$\begin{cases} \vec{E}_n = e^{j\omega t} \left\{ A_n e^{-jk_n(x-x_n)} + B_n e^{jk_n(x-x_n)} \right\} \vec{e}_y \\ \vec{H}_n = \dfrac{j}{\omega\mu_n} \nabla \times \vec{E}_n = \dfrac{j}{\omega\mu_n} \dfrac{\partial E_{ny}}{\partial x} \vec{e}_z = \dfrac{k_n}{\omega\mu_n} e^{j\omega t} \left\{ A_n e^{-jk_n(x-x_n)} - B_n e^{jk_n(x-x_n)} \right\} \vec{e}_z \end{cases} \tag{2.22}$$

Apply boundary conditions at $x = x_{n+1}$, we have:

$$\begin{cases} A_n e^{-jk_nL_n} + B_n e^{jk_nL_n} = A_{n+1} + B_{n+1} \\ k_n A_n e^{-jk_nL_n} - k_n B_n e^{jk_nL_n} = k_{n+1} A_{n+1} - k_{n+1} B_{n+1} \end{cases} \tag{2.23}$$

Equation (2.23) can be rewritten in matrices form:

$$\underbrace{\begin{bmatrix} 1 & 1 \\ k_n & -k_n \end{bmatrix}}_{D_n^{TE}} \underbrace{\begin{bmatrix} e^{-jk_nL_n} & 0 \\ 0 & e^{jk_nL_n} \end{bmatrix}}_{P_n^{TE}} \begin{bmatrix} A_n \\ B_n \end{bmatrix} = \underbrace{\begin{bmatrix} 1 & 1 \\ k_{n+1} & -k_{n+1} \end{bmatrix}}_{D_{n+1}^{TE}} \begin{bmatrix} A_{n+1} \\ B_{n+1} \end{bmatrix} \tag{2.24}$$

Then the transfer matrix of the nth layer can be obtained as:

$$T_n^{TE} = \left[D_{n+1}^{TE} \right]^{-1} D_n^{TE} P_n^{TE} \tag{2.25}$$

The EM field within the last layer of the sensor head can be obtained by the transfer matrices as:

$$\begin{bmatrix} A_N \\ B_N \end{bmatrix} = T_{N-1}^{TE} \cdots T_n^{TE} \cdots T_1^{TE} \begin{bmatrix} A_1 \\ B_1 \end{bmatrix} \tag{2.26}$$

The EM field in the incidence layer is expressed as:

$$\begin{cases} E_{iy} = e^{j\omega t} \left\{ A_i e^{-jk_i(x-x_1)} + B_i e^{jk_i(x-x_1)} \right\} \\ H_{iz} = \dfrac{k_i}{\omega \mu_i} e^{j\omega t} \left\{ A_i e^{-jk_i(x-x_i)} - B_i e^{jk_i(x-x_1)} \right\} \end{cases} \tag{2.27}$$

Apply boundary conditions at $x = x_1$, we have:

$$\begin{cases} A_i + B_i = A_1 + B_1 \\ k_i A_i - k_i B_i = k_1 A_1 - k_1 B_1 \end{cases} \tag{2.28}$$

which again can be rewritten in the form of matrices:

$$\begin{bmatrix} A_1 \\ B_1 \end{bmatrix} = \begin{bmatrix} 1 & 1 \\ k_1 & -k_1 \end{bmatrix}^{-1} \begin{bmatrix} 1 & 1 \\ k_i & -k_i \end{bmatrix} \begin{bmatrix} A_i \\ B_i \end{bmatrix} = \left[D_1^{TE} \right]^{-1} D_i^{TE} \begin{bmatrix} A_i \\ B_i \end{bmatrix} \tag{2.29}$$

Similarly, apply boundary conditions at $x = x_t$, we have:

$$\begin{bmatrix} A_t \\ B_t \end{bmatrix} = \begin{bmatrix} 1 & 1 \\ k_t & -k_t \end{bmatrix}^{-1} \begin{bmatrix} 1 & 1 \\ k_N & -k_N \end{bmatrix} \begin{bmatrix} e^{-jk_N L_N} & 0 \\ 0 & e^{jk_N L_N} \end{bmatrix} \begin{bmatrix} A_N \\ B_N \end{bmatrix} = \left[D_t^{TE} \right]^{-1} D_N^{TE} P_N^{TE} \begin{bmatrix} A_N \\ B_N \end{bmatrix} \quad (2.30)$$

Then we can obtain the total TE transfer matrix for this multi-layered structure as:

$$T_{TE} = \left[\left(D_t^{TE} \right)^{-1} D_N^{TE} P_N^{TE} \right] T_{N-1}^{TE} \cdots T_n^{TE} \cdots T_1^{TE} \left[\left(D_1^{TE} \right)^{-1} D_i^{TE} \right] \quad (2.31)$$

The total reflected EM field can be expressed in terms of the transmitted EM field as:

$$\begin{bmatrix} A_i \\ B_i \end{bmatrix} = \left(T_{TE} \right)^{-1} \begin{bmatrix} A_t \\ B_t \end{bmatrix} = \begin{bmatrix} \left(T_{TE}^{-1} \right)_{11} & \left(T_{TE}^{-1} \right)_{12} \\ \left(T_{TE}^{-1} \right)_{21} & \left(T_{TE}^{-1} \right)_{22} \end{bmatrix} \begin{bmatrix} A_t \\ B_t \end{bmatrix} \quad (2.32)$$

Only outgoing uniform EM wave exists in the transmission layer, i.e. $B_t = 0$.

Assume $A_t = 1$, then we have:

$$\begin{bmatrix} A_i \\ B_i \end{bmatrix} = \begin{bmatrix} \left(T_{TE}^{-1} \right)_{11} \\ \left(T_{TE}^{-1} \right)_{21} \end{bmatrix} \quad (2.33)$$

The total effective reflection coefficient for this multi-layered structure is given by:

$$R = \left| \frac{B_i}{A_i} \right|^2 = \left| \frac{\left(T_{TE}^{-1} \right)_{21}}{\left(T_{TE}^{-1} \right)_{11}} \right|^2 = \left| \frac{\left(T_{TE} \right)_{21}}{\left(T_{TE} \right)_{22}} \right|^2 \quad (2.34)$$

Following the above procedures, we can calculate the exact reflection intensity for each wavelength, and further obtain the exact reflection spectrum for such OFDR based sensor with any number of sensing surfaces.

Now we perform a simulation example to illustrate the sensing principle step-by-step. In this example, a piece of reference wafer and three pieces of identical sensing wafers are bonded together as the sensor head, as seen in Figure 2-13. The sensor head material is

fused silica approximately with a refractive index of 1.46 at room temperature (20 ℃). The thickness of the reference wafer is $d_0 = 10mm$, the thickness of all other three wafers are of the same value $d = 1.5mm$, the depth of the etched air cavity is $d_a = 0.8\mu m$ for all the three sensing wafers.

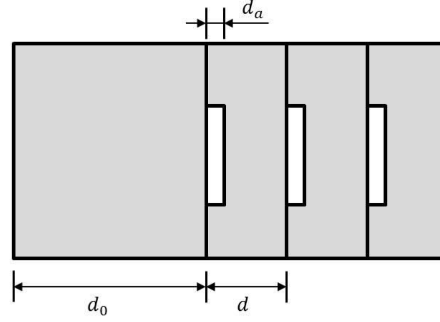

Figure 2-13: Schematic of sensor head structure in the simulation example

As compared to the above general sensor model, there are 7 layers in this sensor head, the thickness of the first layer is $L_1 = 10mm$, the thickness of all even layers is $L_{2m} = d_a = 0.8\mu m$ $(m = 1,2,3)$, the thickness of all odd layers except for the first layer is $L_{2m+1} = d - d_a = 1.5mm - 0.8\mu m$ $(m = 1,2,3)$.

Given the structure of this example, we have the following matrices:

$$
\begin{aligned}
D_a &= D_i^{TE} = D_t^{TE} = D_{2m}^{TE} = \begin{bmatrix} 1 & 1 \\ k & -k \end{bmatrix}, m = 1,2,3 \\
D_s &= D_{2m+1}^{TE} = \begin{bmatrix} 1 & 1 \\ nk & -nk \end{bmatrix}, m = 0,1,2,3 \\
P_1 &= P_1^{TE} = \begin{bmatrix} e^{-jnkL_1} & 0 \\ 0 & e^{jnkL_1} \end{bmatrix} \\
P_a &= P_{2m}^{TE} = \begin{bmatrix} e^{-jkL_{2m}} & 0 \\ 0 & e^{jkL_{2m}} \end{bmatrix}, m = 1,2,3 \\
P_s &= P_{2m+1}^{TE} = \begin{bmatrix} e^{-jnkL_{2m+1}} & 0 \\ 0 & e^{jnkL_{2m+1}} \end{bmatrix}, m = 1,2,3
\end{aligned}
\tag{2.35}
$$

The transfer matrix for the first layer is:

$$T_1 = T_1^{TE} = D_a^{-1} D_s P_1 \tag{2.36}$$

The transfer matrices for all even layers (air cavity) are the same:

$$T_a = T_{2m}^{TE} = D_s^{-1} D_a P_a,\ m = 1,2,3 \tag{2.37}$$

The transfer matrices for all odd layers except for the first layer are the same:

$$T_s = T_{2m+1}^{TE} = D_a^{-1} D_s P_s,\ m = 1,2,3 \tag{2.38}$$

The total transfer matrix for this sensor head structure can be calculated as:

$$T_{TE} = \left(T_s T_a\right)^3 T_1 \left(D_s^{-1} D_a\right) \tag{2.39}$$

This result can be easily extended to such a sensor head structure with any number of sensing wafers, as long as all the etched sensing wafers are identical. For example, if the sensor head consists of (N-1) pieces of sensing wafers, there will be (2N+1) layers, and the total transfer matrix for this general sensor head structure is:

$$T_{TE} = \left(T_s T_a\right)^N T_1 \left(D_s^{-1} D_a\right) \tag{2.40}$$

We can easily set up a computer program based on the above calculation, which is applicable in calculations of reflection spectra for such sensor head structure with any number of sensing wafers.

The output wavelength of the CTS is continuously swept from 1520nm to 1570nm at 5Hz with a resolution of 2.5pm. The reflection intensity at each wavelength can be calculated with Equation (2.39), and the total reflection spectrum is then obtained as shown in Figure 2-14.

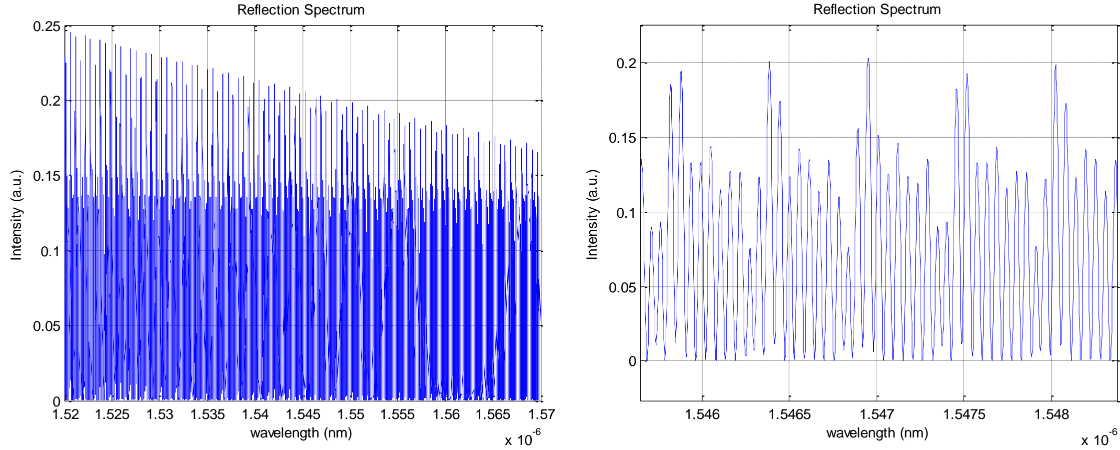

Figure 2-14: Reflection spectrum during a wavelength scan

The next step is to convert the above spectrum from the wavelength domain to the wavenumber domain using the linear interpolation technique, and perform the fast Fourier transform (FFT). The FFT spectrum in spatial domain is shown in Figure 2-15. The peak locations are as expected: the three peaks corresponding to inter-sensor interferences are located at 4.38mm, 8.76mm, and 13.14mm; the four peaks corresponding to reference-sensor interferences are located at 29.2mm, 33.58mm, 37.96mm, and 42.34mm, which are consistent with the OPD values between each sensor surface and the reference surface. The central frequencies for the four reference-sensor peaks are 0.06121, 0.07041, 0.07951, and 0.08871. We then use a digital FIR band-pass filter with a central frequency of 0.08871 to recover the spectrum for the last sensor surface. The recovered spectrum data is truncated to eliminate the distortion caused by the filtering process. The corresponding theoretical spectrum can be obtained by calculating the reflection spectrum for a single piece of fused silica wafer with thickness of 14.5mm ($d_0 + 3d = 10mm + 3 \times 1.5mm = 14.5mm$). The recovered spectrum and theoretical calculated spectrum are plotted on one figure for comparison. As shown in Figure 2-16, the recovered spectrum is consistent with the theoretical spectrum, from which we can demodulate its frequency, i.e. OPD, with high precision.

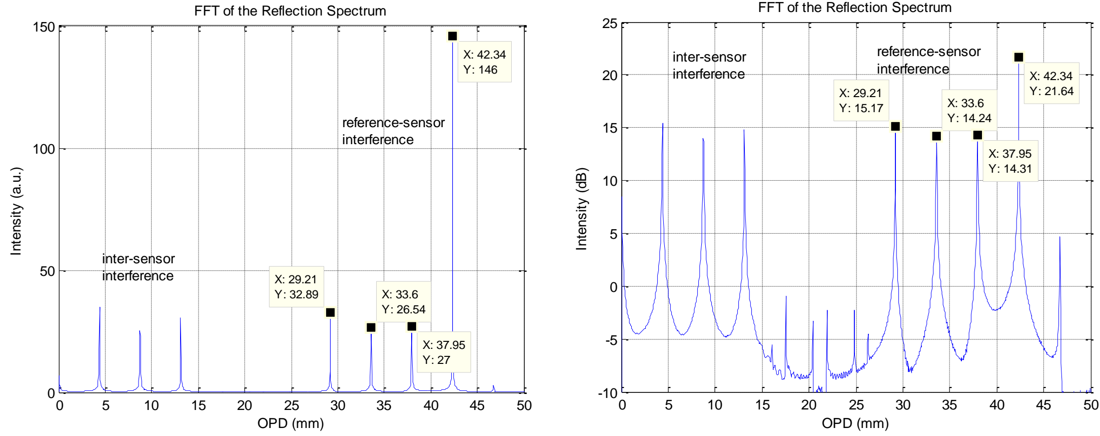

Figure 2-15: Reflection spectrum in spatial domain

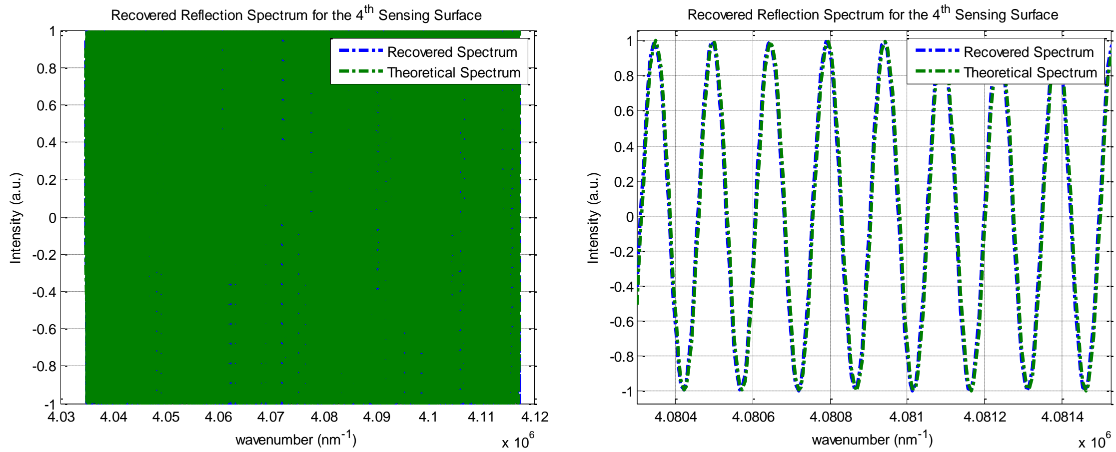

Figure 2-16: Recovered spectrum for the last sensing surface

We can recover the spectra for all other sensing surfaces by simply repeating the above processes with different central frequencies for the band-pass filter.

The OPD value for each sensor will then be obtained by applying linear regression method for the total phase of the corresponding analytical signal as discussed in Section 2.5.

Now we assume the fused silica has a constant thermal coefficient of the refractive index as $\alpha_n = 2.5 \times 10^{-5}$ / ℃, and a constant thermal expansion coefficient as $\alpha_l = 5.5 \times$

10^{-7} / ℃ . With Equation (2.4), we can get an identical theoretical normalized temperature response equation for all the sensing surfaces regardless of the wafer thickness, as long as all wafers are of the same material.

$$\frac{OPD(T)}{OPD(T_0)} \approx 1 + \left(2.5\times10^{-5} + 5.5\times10^{-7}\right)(T - T_0) \tag{2.41}$$

In this simulation, we set the temperature to increase from 20 ℃ to 1000 ℃. The temperature response curves for all four sensing surfaces are plotted together within the left figure of Figure 2-17, and their normalized temperature responses with respect to their OPD values at 20 ℃ are shown in the right figure, which are obviously identical.

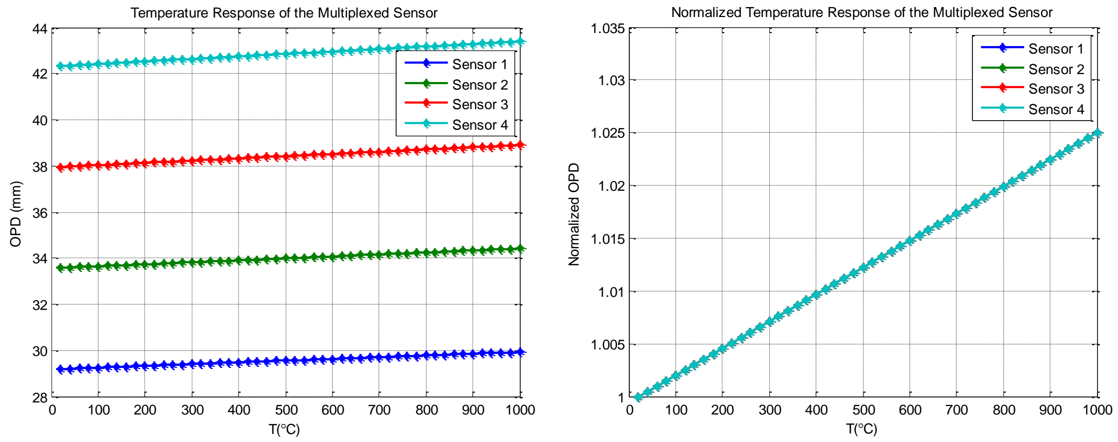

Figure 2-17: Temperature response for all four sensing surfaces (left) and normalized temperature response (right)

The normalized calibration equation for this temperature sensing system is then given as:

$$T = T_0 + \frac{1}{(\alpha_n + \alpha_l)} \frac{OPD(T)}{OPD(T_0)} - 1 \tag{2.42}$$

where α_n and α_l are parameters that only depend on the sensor head material. Equation Chapter (Next) Section 1

Chapter 3
Sensor Head Fabrication

Sensor head is the core element in the whole sensing system. The fabrication of the sensor head will greatly impact on the sensor performance. As mentioned in Chapter 2, we first need to etch a well on one side of all the sensing wafers, which can be realized by a photolithography technique. Then the direct wafer bonding process is taken to fabricate the sensor head, which has relatively high requirements on the quality of the wafer surfaces. In this chapter, the detailed fabrication procedures are presented for both fused silica wafer based sensor head and sapphire wafer based sensor head.

3.1 Sensor Head Materials

As presented in Chapter 2, sapphire wafers are more desirable in practical ultrahigh temperature sensing environment. However, those commercially available sapphire wafers are too thin to be used to construct a distributed sensor for practical applications, and meanwhile customized sapphire rods are too expensive for our current stage of feasibility demonstration of the sensing principle. Instead, the thick fused silica wafers can be custom made at a reasonable price.

We ordered some 2mm and 4mm thick double-side-polished (40/20 scratch/dig) fused silica wafers, with the surface dimension as 10mm×10mm, the parallelism smaller than 1 arc min, and the surface flatness as $\lambda/4$ at 633nm. One piece of 2mm thick wafer will be used as the reference wafer, and 4mm thick wafers will be used as the sensing wafers.

As there are some 330μm thick sapphire wafers with surface dimension as 8mm ×8mm available in our lab, we will also use them to fabricate a sapphire-wafer-based sensor head. Since the sapphire wafers are only available in one thickness, the peaks from the inter-sensor interferences will overlap with those from the reference-sensor interferences in the spatial domain. However, the experimental result shows that the OPD values can still be well demodulated as the thickness differences between the bonded wafers are too

small to affect the signal demodulation. Such sensor structure with identical wafers will not be employed in practical applications, yet can be used for our current stage.

The fabrication procedures are a little different for the fused silica wafer based sensor head and the sapphire wafer based sensor head, which will be presented later.

3.2 Sensor Head Fabrication

Literally, we can bond as many wafers as we want to construct a long distributed sensor. However, as more wafers are cascaded, more accumulated optical light intensity loss would be experienced by the last sensor whose reflection may not be effectively detected due to the insufficient intensity. This challenge would be solved by carefully choosing the depth of the etched air cavity, as shown in later discussions.

3.2.1 Etching of the Well

As mentioned in the previous chapter, we need to etch a well on one side of the wafers before performing the direct wafer bonding process. There two available etching techniques to etch the fused silica wafers: wet etching with hydrofluoric acid (HF) or buffered oxide etch (BOE), and reactive-ion etching (RIE) with fluorine (F) based plasma. And the RIE with chlorine (Cl) based plasma is suitable for etching the sapphire wafers. As compared to RIE, the wet etching is much cheaper, but less controllable or repeatable. It is also very challenging to make a suitable mask for wet etching as the process is usually isotropic which requires full coverage of the wafer except for the area to be etched. Considering all these factors, we will employ RIE to etch both fused silica wafers and sapphire wafers. The etched pattern in the RIE process is defined by a mask which can be either photoresist, or other materials.

3.2.1.1. Determination of Etching Depth

As mentioned earlier, the depth of the etched well will have an impact on the interference intensity, which should be determined before the fabrication process.

As the air cavity between two adjacent bonded surfaces is very thin as compared to the thickness of the wafers, the interference between two surfaces of the air cavity will not affect the signal demodulation for the desired frequencies. However, such interference does have an impact on the measured reflection intensity. As shown in Figure 3-1, the air cavity can also be treated as a FP cavity. If the light beams reflected by two surfaces of the air cavity interfere destructively, more light will be transmitted through the air cavity, and the corresponding peak intensity at the location of this air cavity will be weak. On the other hand, if constructive interference takes place between the two surfaces of the air cavity, the corresponding peak intensity at the location of this air cavity will be strong, and less light will be transmitted through the air cavity. If the sensor head consists of many wafers, the destructive interferences between two surfaces of the air cavity may be desired, so that the reflected intensity from the end surface of the sensor head will be strong enough to be detected with a reasonable signal to noise ratio (SNR).

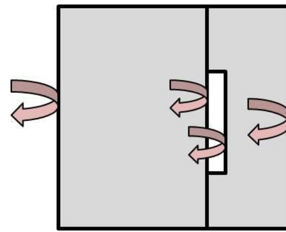

Figure 3-1: Illustration of the reflection from each surface

Considering the half wave loss when light goes from optically thinner medium to optically denser medium (in this case, the half wave loss happens when light goes from air to the wafer), the condition of the air cavity length d_a for the destructive interference between the two surfaces of the air cavity is:

$$d_a = \frac{m\lambda}{2} \tag{3.1}$$

The condition for the constructive interference is:

$$d_a = \frac{(2m-1)\lambda}{4} \tag{3.2}$$

where m is a positive integer.

The following simulation results show consistency with the above analysis.

The schematic of the simulated structure is shown in Figure 3-2. The sensor head consists of one reference wafer with a thickness of $d_0 = 2mm$, and seven identical sensing wafers with the same thickness of $d = 4mm$. All wafers are made of identical material with a refractive index of $n = 1.46$. We vary the air gap thickness d_a in the simulation to shown its impact on the reflection spectrum in the spatial domain. The output wavelength of the light source is linearly swept from 1520nm to 1570nm, with a step of 2.5pm.

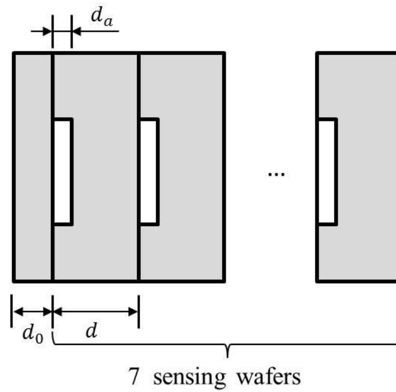

Figure 3-2: Sensor head structure for simulation on the impact of d_a

We choose $d_a = 0.4\mu m, 0.8\mu m, 1.2\mu m, and\ 1.5\mu m$, which are approximately equal to $\lambda/4, \lambda/2, 3\lambda/4, and\ \lambda$ respectively. According to our analysis, $d_a = 0.8\mu m\ and\ 1.5\mu m$ should correspond to an approximately destructive interference between two surfaces of the air cavity; while $d_a = 0.4\mu m\ and\ 1.2\mu m$ should correspond to an approximately constructive interference between two surfaces of the air cavity. Take FFT of the reflection spectra for the above four conditions, the spatial domain spectra are shown in Figure 3-3.

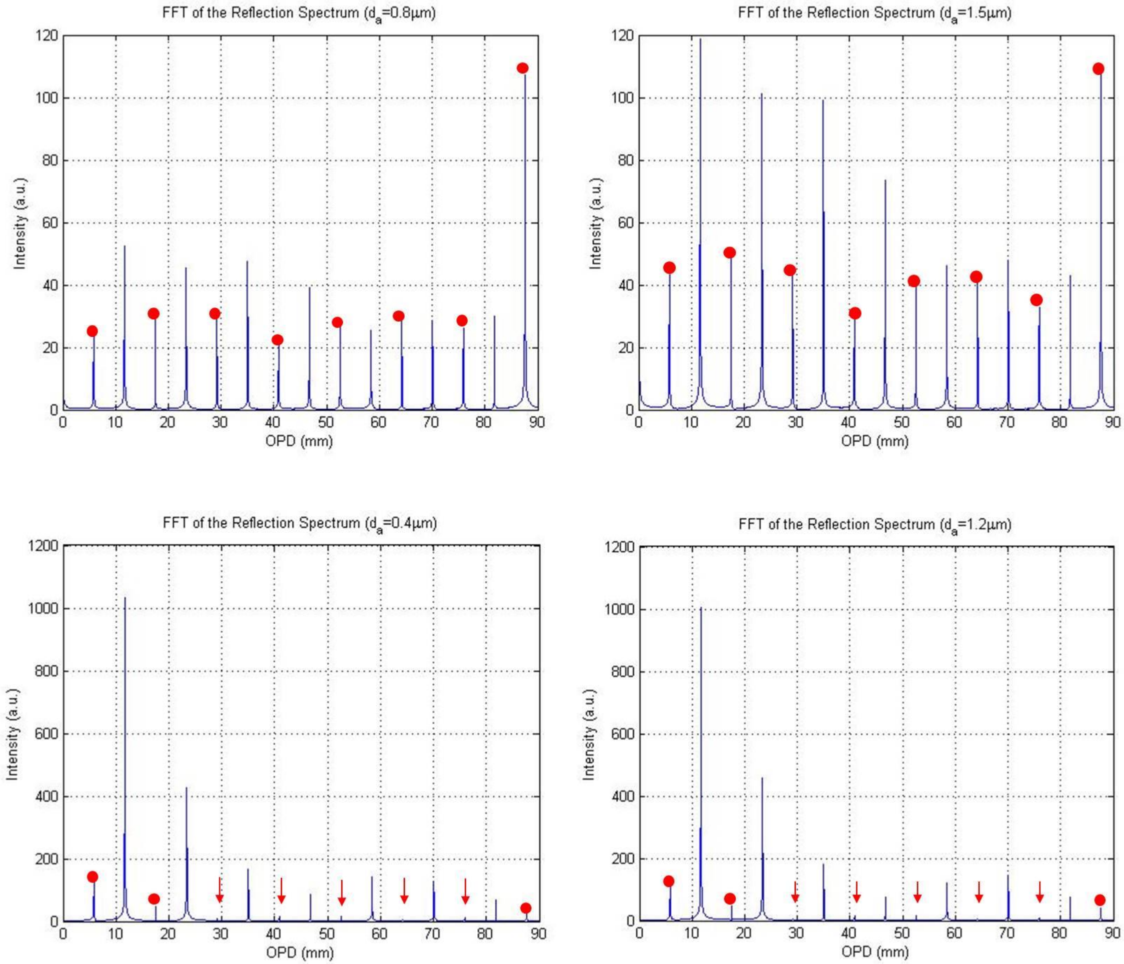

Figure 3-3: FFT results for $d_a = 0.8\mu m$ (upper left), $1.5\mu m$ (upper right), $0.4\mu m$ (lower left), $1.2\mu m$ (lower right)

The simulation results show that when destructive interference takes place between the two surfaces of the air cavity, the peaks at desired locations all possess relatively strong intensities; while in the case of constructive interference, the peak intensity will become weaker if the sensor is placed further away from the reference surface, making the detection ineffective.

3.2.1.2. Etching of Fused Silica Wafers

Photolithography is applied in this work to pattern on fused silica wafers. It uses UV light to transfer a certain pattern from a photo-mask to photoresist. The basic procedures in the photolithography include cleaning, preparation, photoresist application, exposure and developing, etching, and photoresist removal, as shown in Figure 3-4.

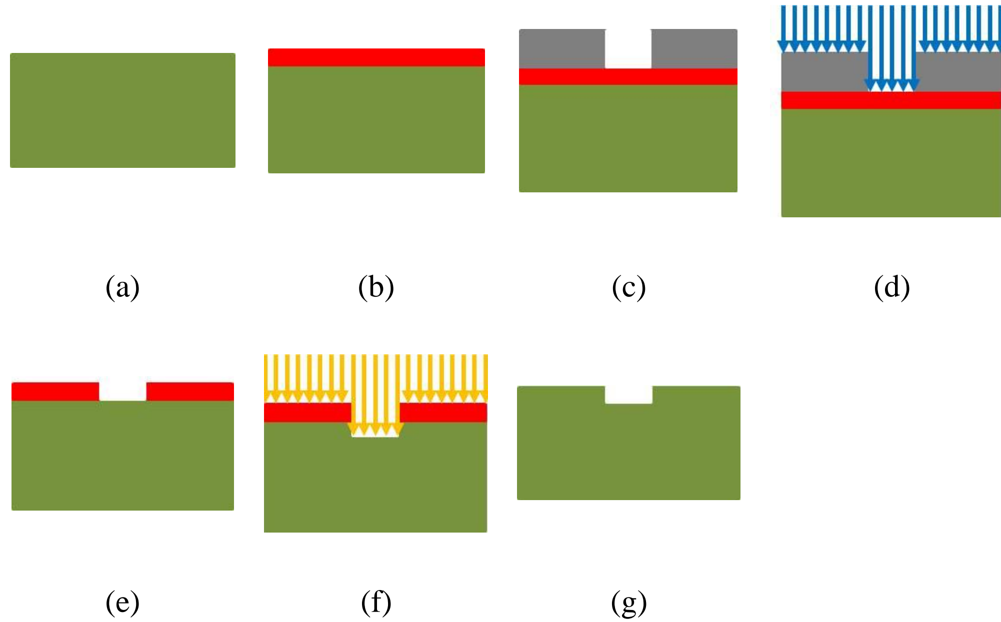

Figure 3-4: Simplified illustration of photolithography

We first clean the fused silica wafers with Nano-Strip, which is a stabilized mixture of sulfuric acid and hydrogen peroxide to remove the organic and inorganic contaminations, at 60 ℃. After cleaning, the wafers are baked at 100 ℃ for around 30 minutes to sufficiently drive off any moisture that may present on the wafer surface (Figure 3-4 (a)).

After the preparation of the fused silica wafers, we next apply the photoresist by spin coating (Figure 3-4 (b)). Figure 3-5 (a) is the picture of the spin coater we used to apply the photoresist. The photoresist used in our fabrication is AZ9260 which is a thick film positive photoresist and suitable for the following RIE process. The spin coating first runs at 500 rpm for 15 seconds, and then runs at 2000 rpm for 30 seconds, producing a photoresist layer with thickness between $10\mu m$ to $12\mu m$ as measured with a Dektak

profilometer. The photoresist-coated fused silica wafers are then prebaked at 120 ℃ for 10 minutes to drive off excess photoresist solvent.

(a) (b) (c)

Figure 3-5: (a) Spin coater; (b) MA6 mask aligner; (c) Photo-mask

After prebaking, we use the MA6 mask aligner (as shown in Figure 3-5 (b)) to align the photo-mask and do the exposure for around 40 seconds (Figure 3-4 (c), (d)). The photo-mask is printed on a transparent plastic paper, and cut to fit the 4-inch optical glass attached to the mask holder, as shown in Figure 3-5 (c). A mixture of the developer AZ400K and deionized (DI) water at a ratio of 1:4 is then used for developing the exposed wafers to remove the photoresist on the exposed area (Figure 3-4 (e)). This developing process typically takes around 3 minutes, and the geometric pattern on the photo-mask is then transferred to the photoresist. The wafers are then hard-baked at 120 ℃ for 5 minutes to solidify the remaining photoresist and make it more durable for the following etching process.

A Trion MiniLock RIE system with an inductively coupled plasma (ICP) source (as shown in Figure 3-6) is used to perform the dry etching process (Figure 3-4 (f)). The plasma etchant for fused silica wafers is CHF_3 with a flow rate of 50 sccm, and pressure of 50 mTorr. The ICP RF power is 350 W, and the RIE RF power is 100 W. With this

recipe, the etching rate of our fused silica wafers is around 100 nm/min. An 8 minutes' process will yield a 0.8 μm deep cavity in the fused silica wafers.

Figure 3-6: Trion MiniLock reactive ion etching system

After the etching process, the residual photoresist is removed by acetone first, and then the wafers are put into the Nano-Strip solution for further cleaning (Figure 3-4 (g)).

3.2.1.3. Etching of Sapphire Wafers

The sapphire wafers are first cleaned by Nano-Strip which is similar to the cleaning of fused silica wafers.

Instead of using the photoresist as the mask layer, we use a piece of glass slide with a certain pattern as our physical mask for sapphire wafers, because the etching rate for sapphire wafers is relatively slow based on the chosen recipe which will be presented later, and our current available photoresist are not thick enough to stand though the whole process duration.

To make the mask, we first cut the glass slide to be slightly larger than the sapphire wafer; and then wax the whole glass slide and leave it with a 2.5mm by 2.5mm square in the

center on both sides; the waxed glass slide is then etched by the hydrofluoric acid (HF) to form a through-hole in the center. After patterned on the glass slide, the wax is removed.

The glass slide mask is attached to the sapphire wafer by the thermal conductive paste. The other side of the sapphire wafer is then attached onto a silicon wafer by the same paste, as shown in Figure 3-7. The thermal conductive paste helps dissipate heat generated during the etching process. The silicon wafer is then placed onto the wafer platter of the RIE system for further processes.

Figure 3-7: Configuration of sapphire wafers and masks for RIE

The plasma etchant for sapphire wafers is a mixture of 80% BCl_3 and 20% Cl_2 with a total flow rate of 40 sccm, and pressure of 10 mTorr. The ICP RF power is 300 W, and the RIE RF power is 200 W [33]. An etching rate of 30 nm/min is reported in [34]. The etched depth measured by the Dektak profilometer is about $1\mu m$. As only three pieces of sapphire wafers will be used to make the sensor head in the following procedure, the etching depth is not a concern in this case.

3.2.2 Direct Bonding

After the etched wafers are prepared, we next directly bond the reference wafer and the etched sensing wafers to form the sensor head.

The direct bonding process is based on chemical bonds between two surfaces.

Before bonding two wafers, we first need to clean the wafers to remove any impurities. And then a hydrogen based pre-bonding process is performed after the cleaning, followed by a stronger diffusion-based bonding at an elevated temperature. The detailed processes are a little different for fused silica wafers and sapphire wafers.

The bonding processes for fused silica wafers are as follows:

- Clean the fused silica wafers with DI water for 30 minutes.
- Clean the fused silica wafers with acetone for 30 minutes.
- Clean the fused silica wafers with piranha solution which is a mixture of 3:1 concentrated sulfuric acid (H_2SO_4) to 30% hydrogen peroxide (H_2O_2) at 60 ℃ for 45 minutes.
- Pre-bond the fused silica wafers at 200 ℃ for 50 minutes.
- Bake the pre-bonded fused silica wafers at 850 ℃ with certain weight applied for over 50 hours, and then annealed at 850 ℃ with no applied weight to release the internal stresses [35].

The bonding processes for sapphire wafers are as follows [34]:

- Clean the sapphire wafers with DI water for 30 minutes.
- Clean the sapphire wafers with acetone for 30 minutes.
- Clean the sapphire wafers with piranha [32] solution at 60 ℃ for 45 minutes.
- Clean the sapphire wafers with 85% H_3PO_4 at 150 ℃ for 45 minutes.
- Immerse the sapphire wafers into diluted H_2SO_4 solution for 15 minutes to deposit a hydrophilic OH^- layer.
- Pre-bond the sapphire wafers at 200 ℃ for 50 minutes.
- Bake the pre-bonded sapphire wafers at 1200 ℃ with certain weight applied for over 50 hours, and then annealed at 1200 ℃ with no applied weight to release the internal stresses [35].

During the pre-bonding processes for both fused silica wafers and sapphire wafers, a clamping vise is used to apply pressure on the wafers to help eliminate any gap between two surfaces.

The bonding of three pieces of sapphire wafers turned out to be successful, while unfortunately the pre-bonding of four pieces of fused silica wafers failed, as shown in Figure 3-8. The two pieces of fused silica wafers at the bottom are bonded, while the top two pieces are not. The failure of the wafer bonding may be caused by inadequate surface quality of the wafers, contamination of the wafer surfaces, and/or unevenly applied pressure. Since the holder is made of aluminum which has a much larger thermal expansion coefficient than the fused silica, direct contact between the fused silica wafers and the holder may cause cracks on fused silica wafers. A piece of rubber can be used on all contacting surfaces to protect the wafers, and also transfer the pressure onto the wafers more evenly. Further studies need to be taken on the bonding processes of fused silica wafers.

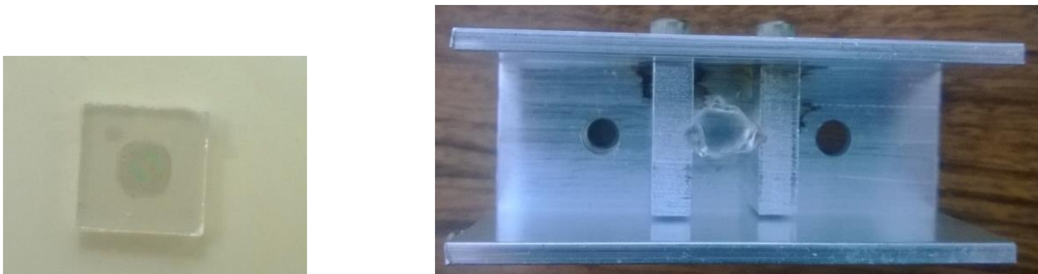

Figure 3-8: Bonding results: sapphire sensor head (left), fused silica wafers (right)

Equation Chapter (Next) Section 1

Chapter 4
Evaluation of Sensor Performance

Chapter 3 presented the detailed fabrication processes of the sensor head. As the bonding of fused silica wafers was failed, we will only evaluate the performance of the sapphire wafer based sensor head in this chapter. The sensor head is fabricated from direct bonding of three pieces of 330μm thick sapphire wafers. The structure dimensions are shown in Figure 4-1.

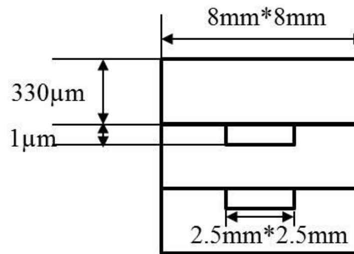

Figure 4-1: Structure of sapphire wafer based sensor head

4.1 Experimental Test Setup

The schematic of this laboratory experiment setup is shown in Figure 4-2. Light is emitted from the CTS, and propagates to the collimator through a fiber circulator. The collimated light beam propagates to the sensor head through free space. And the reflected light by the sensor head is coupled back into the collimator and received by the built-in photo-detector of the CTS through the fiber circulator. The sensor head is placed in a furnace, and a thermocouple is placed adjacently to the sensor head as the temperature reference. Since the sapphire wafers used in the sensor head are thin, there will be no obvious temperature gradients between the three wafers. The readings of the thermocouple can be used as reference temperatures for all three wafers.

The sensor calibration was taken from room temperature to 1000 ℃, and spectra data were read at intervals of 100 ℃.

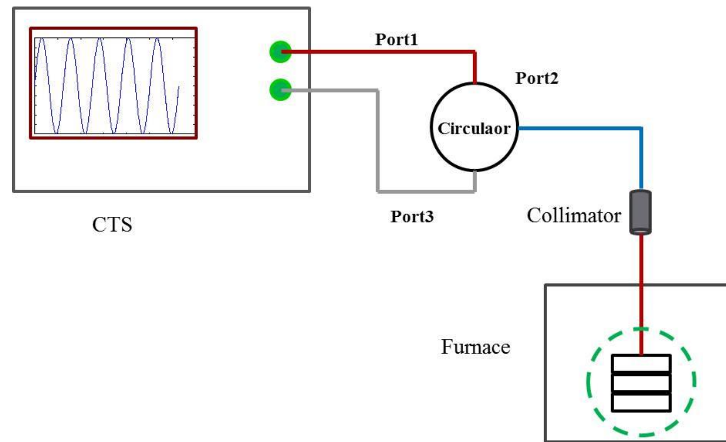

Figure 4-2: Schematic of experiment setup for temperature calibration

4.2 Signal Demodulation

Figure 4-3 shows the measured reflection spectrum from the photo-detector of the CTS during one sweep cycle at room temperature in logarithmic scale. The FFT of this reflection spectrum in spatial domain is plotted in both linear and logarithmic scale as seen in Figure 4-4. The first three peaks are corresponding to the reference-sensor interferences, and all of them have excellent signal to noise ratios (SNR).

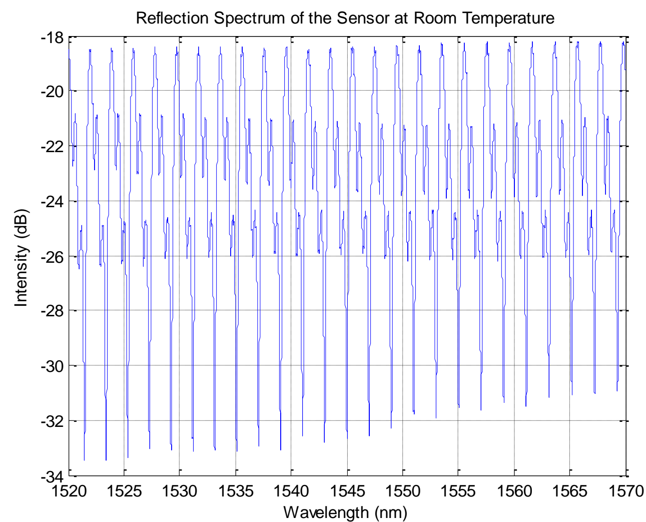

Figure 4-3: Reflection spectrum of the sensor measured at room temperature

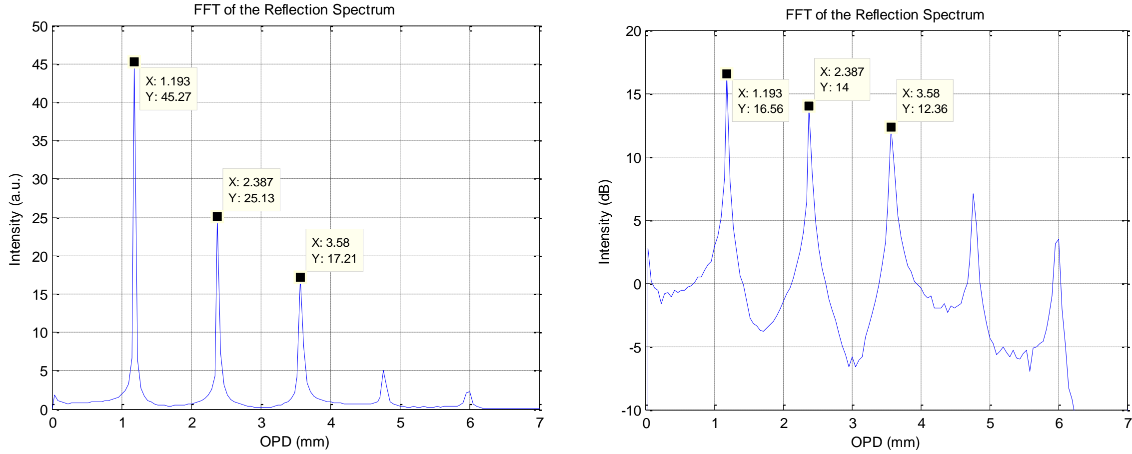

Figure 4-4: Reflection spectrum of the sensor in spatial domain

Now we can apply digital filters to select each peak and recover the reflection spectrum for each sensor, as presented in detail in Chapter 2. The recovered reflection spectra for all three sensors are plotted together in Figure 4-5. It is clear that the reflection spectra are perfectly recovered for all three sensors.

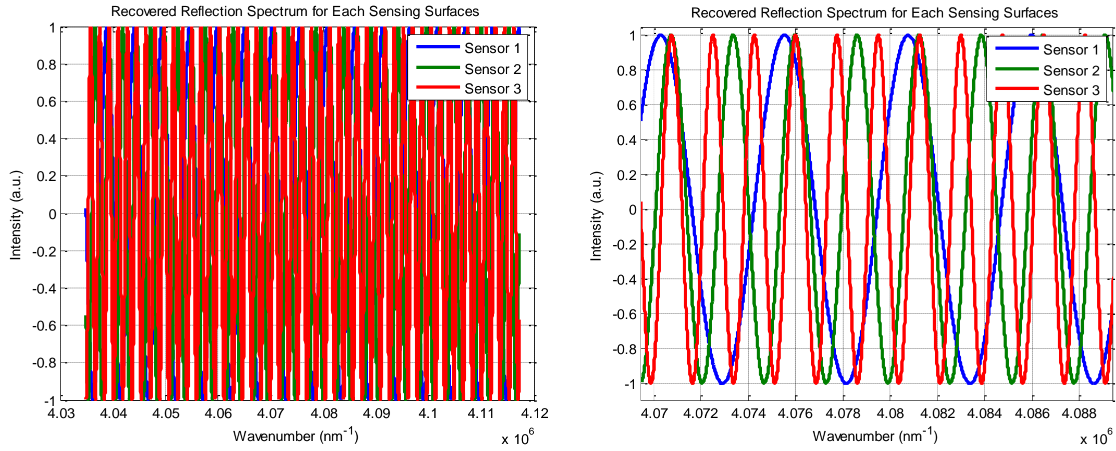

Figure 4-5: Recovered spectra for all three sensing surfaces

The temperature response curves for all three sensors are plotted in Figure 4-6. Normalize the three temperature response curves to their corresponding OPD values at 100 ℃, the results are shown in Figure 4-7. The normalized temperature response curves for all three

sensors are almost identical, and can be linearly fitted to one temperature response curve as:

$$\frac{OPD(T)}{OPD(T_0 = 100°C)} \approx 1.602 \times 10^{-5} T + 0.9984 \tag{4.1}$$

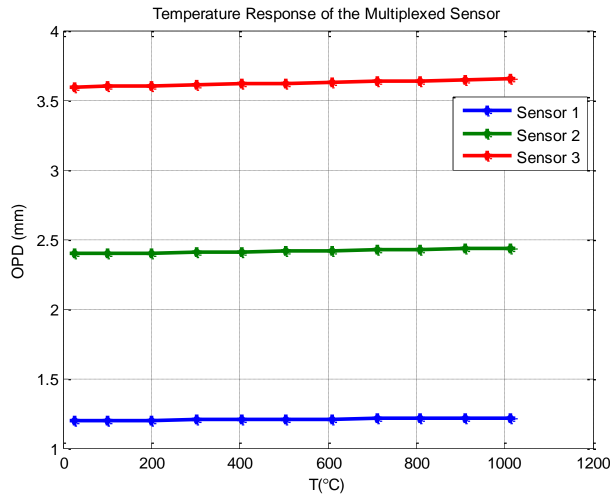

Figure 4-6: Temperature response curves for the multiplexed sensor

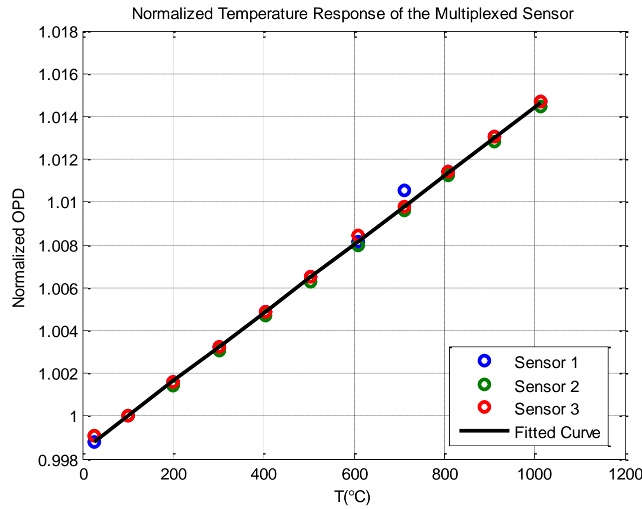

Figure 4-7: Normalized temperature response curves

The sensitivity of the sensor is defined by the slope of the normalized temperature response curve as:

$$S = \frac{d}{dT}\left[\frac{OPD(T)}{OPD(T_0 = 100°C)}\right] = 1.602 \times 10^{-5} / °C \tag{4.2}$$

The resolution is the smallest temperature change that could be resolved by the sensing system [11]. 100 samples were taken at the room temperature, and the standard deviation of the end sensor's OPD value is $\sigma = 39.3nm$, the resolution of the sensor is given as:

$$R = \frac{2\sigma}{S \cdot OPD(T_0 = 100°C)\big|_{Sensor3}} \approx 1.3°C \tag{4.3}$$

The resolution can be further improved by taking more samples during the calibration.

More experiments need to be performed to evaluate the sensor's repeatability.

Although this OFDR based sapphire sensor head was only tested to 1000 ℃, it can potentially operate beyond 1600 ℃.

4.3 Feasibility of Long Distance Interrogation

As mentioned in Chapter 1, this free space sensor interrogation system is desired in harsh environment applications like coal gasifier, where the ambient temperature around the gasifier can be very high. To avoid damage on optical components such as the collimator in the sensor interrogation system, long distance (>1m) interrogation is desired.

As limited by the experimental configuration, the feasibility of long distance interrogation is only demonstrated at room temperature with an interrogation distance of around one meter.

One piece of 5.8mm thick glass and 4 pieces of 1.1mm thick glass slides are stacked together as the sensor head. The reflection spectrum detected by the CTS is shown in Figure 4-8.

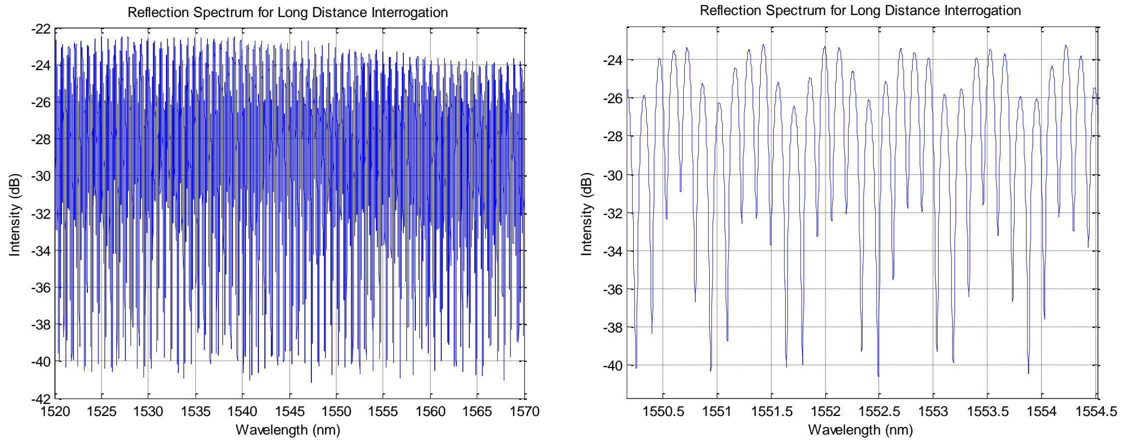

Figure 4-8: Reflection spectrum of this long distance interrogation

The FFT of the detected signal is shown in Figure 4-9. Although the peaks are very weak for sensors that are placed far away from the reference surface, they still have a reasonable SNR as can be seen in the FFT spectrum of logarithmic scale (Figure 4-9 (right)).

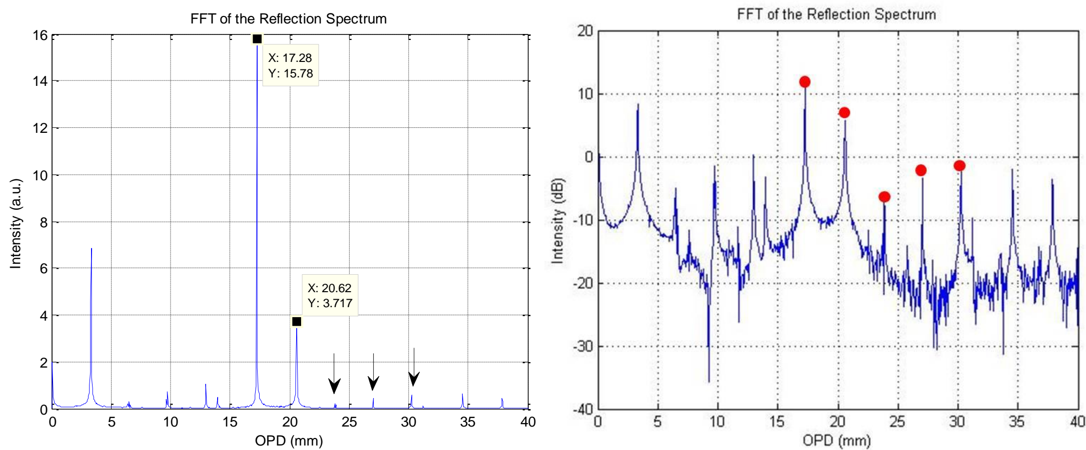

Figure 4-9: FFT of the reflection spectrum

In this preliminary experiment, the glasses were simply stacked and placed in a holder with a screw to press them tightly. The parallelism of these glasses is not as good as those wafers used in our sensor head fabrication. The signal quality can be greatly improved if we test with the fabricated sensor head.

In the long distance interrogation, the light coupled back into the collimator will inevitably experience intensity loss due to light beam divergence. Even though the reflected light can only be partially coupled back into the collimator and detected by the photo-detector, we can still obtain the spectrum with decent SNR. This preliminary result has demonstrated the feasibility of long distance interrogation of our sensing system.

Chapter 5
Conclusion and Future Work

In this thesis, both theoretical and experimental studies have been conducted on an OFDR based multiplexed high temperature sensor. A summary of the completed work and a discussion on recommended future study are provided in this chapter.

5.1 Summary of Work

This work is motivated by the challenge encountered by the optical fiber based sensor link that the shear force caused by the differential thermal expansion between the inner and outer layers of the gasifier refractory to the lead-in sapphire fiber may break the sensor probe, as discussed in Chapter 1. Other than traditional fiber based sensor link, we proposed a free space based interrogation sensing system, of which only the sensor head will be placed in the inner refractory wall of the coal gasifier, while all the other interrogation components are placed in the outer refractory or outside the gasifier.

The design of the whole sensing system is based on OFDR multiplexed sensing technique, as discussed in detail in Chapter 2. By demodulating the temperature dependent OPD values for each sensor, a temperature calibration curve can be obtained. In future sensing applications, the unknown temperature can be easily calculated from the sensor's OPD value by using the calibration curve. In this proposed OFDR based multiplexed sensing system, the reference and sensors are placed in line; as long as each sensor is placed at a different physical distance away from the reference surface, the reference-sensor interference spectra can be easily recovered for each sensor, and further the OPD values for each sensor can be demodulated with certain signal processing technique as discussed in Chapter 2.

In this thesis, we tried to fabricate the sensor head with both fused silica wafers and sapphire wafers by combining the photolithography technique and direct wafer bonding technique. The fabrication of sapphire wafer based sensor head turned out to be a success. This adhesive-free sensor head has shown great performance during the in-lab

experiment. It showed an approximately linear response during the temperature calibration with temperature increased from room temperature to 1000 ℃, and a temperature resolution of about 1.3 ℃ was obtained. The fabrication based on thick fused silica wafers failed during the direct bonding process, which needs further study.

5.2 Suggestions for Future Work

The work performed over the course of this thesis provides a good demonstration for the feasibility of such OFDR based multiplexed temperature sensing. Even so, much work can be done if this research subject should continue.

Current sensor head is fabricated with three pieces of identical sapphire wafers, which have a thickness of only $330\mu m$. Although such structure can be used in this feasibility study, it is not applicable in practical distributed sensing applications, where sensor head with a much longer dimension is desired. Sapphire rods with two ends well-polished are good candidates to fabricate such sensor head.

The direct bonding of thick wafers still remains challenging. Further study needs to be taken on the factors that may cause bonding failure. The failure of fused silica wafer bonding in this work may mainly be caused by the clamp method during the pre-bonding process. A new holder should be designed in a way that more even force can be applied onto the wafer stack, and rubber is suggested as a buffer between the wafer and metallic holder. The success of the direct bonding technique may bring great advantages for such sensor structure, as we can bond as many sensors as possible to realize distributed sensing applications.

References

[1] V. Vali and R. W. Shorthill, "Fiber ring interferometer," *Applied Optics,* vol. 15, pp. 1099-1100, 1976/05/01 1976.

[2] A. J. Rogers, "Optical methods for measurement of voltage and current on power systems," *Optics & Laser Technology,* vol. 9, pp. 273-283, 12// 1977.

[3] H. Y. Choi, K. S. Park, S. J. Park, U.-C. Paek, B. H. Lee, and E. S. Choi, "Miniature fiber-optic high temperature sensor based on a hybrid structured Fabry?Perot interferometer," *Optics Letters,* vol. 33, pp. 2455-2457, 2008/11/01 2008.

[4] X. Wan and H. F. Taylor, "Intrinsic fiber Fabry-Perot temperature sensor with fiber Bragg grating mirrors," *Optics Letters,* vol. 27, pp. 1388-1390, 2002/08/15 2002.

[5] H.-S. Choi, H. F. Taylor, and C. E. Lee, "High-performance fiber-optic temperature sensor using low-coherence interferometry," *Optics Letters,* vol. 22, pp. 1814-1816, 1997/12/01 1997.

[6] J. Jung, H. Nam, B. Lee, J. O. Byun, and N. S. Kim, "Fiber Bragg Grating Temperature Sensor with Controllable Sensitivity," *Applied Optics,* vol. 38, pp. 2752-2754, 1999/05/01 1999.

[7] D. Grobnic, S. J. Mihailov, C. W. Smelser, and D. Huimin, "Sapphire fiber Bragg grating sensor made using femtosecond laser radiation for ultrahigh temperature applications," *Photonics Technology Letters, IEEE,* vol. 16, pp. 2505-2507, 2004.

[8] N. Hirayama and Y. Sano, "Fiber Bragg grating temperature sensor for practical use," *ISA Transactions,* vol. 39, pp. 169-173, 4// 2000.

[9] Z. Huang, G. Pickrell, J. Xu, Y. Wang, Y. Zhang, and A. Wang, "Sapphire temperature sensor coal gasifier field test," 2004, pp. 27-36.

[10] *http://en.wikipedia.org/wiki/Fabry%E2%80%93P%C3%A9rot_interferometer*.

[11] Y. Zhu, *Miniature fiber-optic sensors for high-temperature harsh environments*. Blacksburg, VA: University Libraries, Virginia Polytechnic Institute and State University, 2007.

[12] J. Wang, *Sapphire Fiber Based Sensing Technologies for High Temperature Applications*. Blacksburg, VA: University Libraries, Virginia Polytechnic Institute and State University, 2011.

[13] J. Wang, B. Dong, E. Lally, J. Gong, M. Han, and A. Wang, "Multiplexed high temperature sensing with sapphire fiber air gap-based extrinsic Fabry-Perot interferometers," *Optics Letters,* vol. 35, pp. 619-621, 2010/03/01 2010.

[14] D. G. K. F. P. Kapron, P. M. Garel-Jones, "Aspects of Optical Frequency-Domain Reflectometry," presented at the Technical Digest, Third International Conference on Integrated Optics and Optical Fiber Communication (OSA), Washington, DC, 1981.

[15] W. Eickhoff and R. Ulrich, "Optical frequency domain reflectometry in single-mode fiber," *Applied Physics Letters,* vol. 75, pp. 693-695, 1981.

[16] R. I. MacDonald, "Frequency domain optical reflectometer," *Applied Optics,* vol. 20, pp. 1840-1844, 1981/05/15 1981.

[17] H. Ghafoori-Shiraz and T. Okoshi, "Optical-fiber diagnosis using optical-frequency-domain reflectometry," *Optics Letters,* vol. 10, pp. 160-162, 1985/03/01 1985.

[18] K. Yuksel, M. Wuilpart, V. Moeyaert, Me, x, and P. gret, "Optical frequency domain reflectometry: A review," in *Transparent Optical Networks, 2009. ICTON '09. 11th International Conference on*, 2009, pp. 1-5.

[19] B. Huttner, B. Gisin, O. Guinnard, N. Gisin, R. Passy, and J.-P. Von der Weid, "Optical frequency domain reflectometer for characterization of optical networks and devices," *ComTec,* vol. 77, pp. 20-23, 1999.

[20] J. P. Von der Weid, R. Passy, G. Mussi, and N. Gisin, "On the characterization of optical fiber network components with optical frequency domain reflectometry," *Lightwave Technology, Journal of,* vol. 15, pp. 1131-1141, 1997.

[21] P. Oberson, B. Huttner, O. Guinnard, L. Guinnard, G. Ribordy, and N. Gisin, "Optical frequency domain reflectometry with a narrow linewidth fiber laser," *Photonics Technology Letters, IEEE,* vol. 12, pp. 867-869, 2000.

[22] B. Soller, D. Gifford, M. Wolfe, and M. Froggatt, "High resolution optical frequency domain reflectometry for characterization of components and assemblies," *Optics Express,* vol. 13, pp. 666-674, 2005/01/24 2005.

[23] J. P. Von der Weid, R. Passy, A. O. Forno, B. Huttner, and N. Gisin, "Return loss measurements of WDM filters with tunable coherent optical frequency-domain reflectometry," *Photonics Technology Letters, IEEE,* vol. 9, pp. 1508-1510, 1997.

[24] B. Huttner, J. Reecht, N. Gisin, R. Passy, and J. P. Von der Weid, "Local birefringence measurements in single-mode fibers with coherent optical

frequency-domain reflectometry," *Photonics Technology Letters, IEEE,* vol. 10, pp. 1458-1460, 1998.

[25] M. Wegmuller, M. Legre, and N. Gisin, "Distributed beatlength measurement in single-mode fibers with optical frequency-domain reflectometry," *Lightwave Technology, Journal of,* vol. 20, pp. 828-835, 2002.

[26] M. E. Froggatt, D. K. Gifford, S. Kreger, M. Wolfe, and B. J. Soller, "Characterization of Polarization-Maintaining Fiber Using High-Sensitivity Optical-Frequency-Domain Reflectometry," *Journal of Lightwave Technology,* vol. 24, pp. 4149-4154, 2006/11/01 2006.

[27] M. Froggatt and J. Moore, "High-Spatial-Resolution Distributed Strain Measurement in Optical Fiber with Rayleigh Scatter," *Applied Optics,* vol. 37, pp. 1735-1740, 1998/04/01 1998.

[28] S. Yun, G. Tearney, J. de Boer, N. Iftimia, and B. Bouma, "High-speed optical frequency-domain imaging," *Optics Express,* vol. 11, pp. 2953-2963, 2003/11/03 2003.

[29] A. Wang, S. Gollapudi, K. A. Murphy, R. G. May, and R. O. Claus, "Sapphire-fiber-based intrinsic Fabry?Perot interferometer," *Optics Letters,* vol. 17, pp. 1021-1023, 1992/07/15 1992.

[30] B. Qi, G. R. Pickrell, J. Xu, P. Zhang, Y. Duan, W. Peng*, et al.*, "Novel data processing techniques for dispersive white light interferometer," *Optical Engineering,* vol. 42, pp. 3165-3171, 2003.

[31] F. Shen and A. Wang, "Frequency-estimation-based signal-processing algorithm for white-light optical fiber Fabry-Perot interferometers," *Appl. Opt.,* vol. 44, pp. 5206-5214, 09/01 2005.

[32] S. Tretter, "Estimating the frequency of a noisy sinusoid by linear regression (Corresp.)," *Information Theory, IEEE Transactions on,* vol. 31, pp. 832-835, 1985.

[33] C. H. Jeong, D. W. Kim, K. N. Kim, and G. Y. Yeom, "A Study of Sapphire Etching Characteristics Using BCl3-based Inductively Coupled Plasmas," *Japanese Journal of Applied Physics,* vol. 41, pp. 6206-6208, 2002.

[34] J. Yi, E. Lally, W. Anbo, and X. Yong, "Demonstration of an All-Sapphire Fabry–Pérot Cavity for Pressure Sensing," *Photonics Technology Letters, IEEE,* vol. 23, pp. 9-11, 2011.

[35] A. Sugiyama, H. Fukuyama, T. Sasuga, T. Arisawa, and H. Takuma, "Direct bonding of Ti : sapphire laser crystals," *APPLIED OPTICS,* vol. 37, pp. 2407-2410, 1998.